nature water

Article

https://doi.org/10.1038/s44221-023-00139-9

Hybrid photothermal–photocatalyst sheets for solar-driven overall water splitting coupled to water purification

In the format provided by the authors and unedited

Table of Contents

Supplementary Discussion 1 | Justification for materials selection for sheet fabrication.

Aluminium-doped strontium titanate (Al:$SrTiO_3$) was selected as a UV-active PC material due to its high activity toward overall water splitting, simple synthesis and low cost.[1,2] Depending on the co-catalyst and loading method, Al:$SrTiO_3$ can yield overall water splitting with an external quantum efficiency of 68-98% at 350 nm.[3,4] The impregnation technique was utilized for co-catalyst deposition instead of photodeposition, which would provide a higher activity, due to its potential for scalability.[5] The trade-off of this simple fabrication procedure is the inherently lower efficiency of the photocatalyst. The carbon-based gas diffusion layer consisting of a fibrous macroporous bottom layer and a smooth macroporous top layer (Fig. 2c, Supplementary Fig. 3) was selected as the SVG due to three reasons: (i) the light-weight substrate (density ≈ 0.49 g cm^{-3}) is able to float on the liquid surface, (ii) the porous structure of the bottom surface facilitates efficient water transport and (iii) the black colour and light-scattering nature of the top macroporous surface allows for broad-spectrum solar absorption to generate heat (Fig. 1e), while being small enough for deposition of the PC layer.

Supplementary Discussion 2 | Photocatalyst loading optimization.

To investigate the optimum PC powder loading, the photothermal-photocatalyst sheets (photoactive area: 1×1 cm^2) with 0.5–4.0 mg cm^{-2} of $RhCrO_x$-Al:$SrTiO_3$ loading were first prepared and tested on Milli-Q water. The photographs and SEM images show different extent of PC coverage and thickness on the SVG ranging from 1–10 μm (Supplementary Figs. 25–27). Fig. 2d shows that the H_2 produced (per irradiated area) and the solar-to-H_2 (STH) efficiency increases with PC loading and starts to saturate beyond a loading of 2.0 mg cm^{-2}. The highest H_2 evolution rate of 20.6±3.7 mmol m^{-2} h^{-1} (corresponding to an STH efficiency of 0.13±0.02%) was obtained with a catalyst loading of 4.0 mg cm^{-2}. The H_2 produced (per gram catalyst) remains constant up to 2.0 mg PC loading and then starts to decrease significantly due to light shielding by the excess photocatalyst layer formed at high catalyst loadings. (Supplementary Table 16).

Vapour generation was studied in a custom $1.5 \times 1.5 \times 5.0$ cm^3 reactor with an open top (Supplementary Fig. 24). While the bare SVG substrate had a vapour generation rate of 1.07±0.08 kg m^{-2} h^{-1} (compared to a base rate of 0.55±0.11 kg m^{-2} h^{-1} without SVG), the rates obtained by the photothermal-photocatalyst sheets with 0.0–4.0 mg cm^{-2} PC generally decreased from 1.07±0.08 to 0.88±0.15 kg m^{-2} h^{-1}, corresponding to a drop in solar thermal conversion efficiency (η) from 67.7±5.2 to 55.3±9.4%, which agrees well with reported literature values for carbonaceous SVG (Fig. 2e, Supplementary Tables 3). A slight decreasing trend was observed with increasing catalyst loading due to light blocking and scattering by the PC top layer, which suggests that excessive PC loading can negatively impact the SVG performance.

Based on the above results, a trade-off is necessary to balance PC cost, vapour generation rate and overall device activity. A lower catalyst loading allows for material saving and better vapour transport through the PC layer, whereas a higher catalyst loading may enable better thermal insulation and reduce heat losses, at the cost of increasing vapour transport resistance and reducing visible and IR light transmittance. Taking these factors into account, an optimal catalyst loading of 2.0 mg was selected and used in all subsequent experiments. This was primarily due the drop in photocatalytic productivity as indicated by the decrease in H_2 evolution per gram catalyst beyond a catalyst loading of 2.0 mg (Fig. 2d). From an economic standpoint, catalyst loadings above 2.0 mg yield diminishing returns as the cost of additional PC material outweighs the relatively small increase in product H_2. On the other hand, while catalyst loading also affects the vapour generation rate of the PC sheets, this factor was less important as there was only a marginal decrease in vapour generation rate with increasing catalyst loading (Fig. 2e). Furthermore, at all catalyst loadings, the vapour generation rate was well over the water utilization rate by photocatalysis, meaning that the supply of feedstock to the PC layer was not a significant element to consider.

Supplementary Discussion 3 | Performance of SVG-PC versus Glass-PC.

While our SVG-PC system outperformed untreated SVG-PC and Glass-PC (liquid-phase) for seawater splitting, it displayed a ~20% lower H_2 evolution rate than Glass-PC in pure water (Fig. 3a). The reason for the lower activity in vapour-phase water splitting is attributed to the lower water partial pressure, and limited interaction of vapour and the PC surface,[6] which leads to a lower coverage of water molecules on the surface of the photocatalyst.[7] This drop in performance is relatively small compared to other reported gas-phase water splitting systems which see far more substantial declines in performance when replacing liquid water by water vapour.[7,8] In our current design, the constant flux of water vapour passing through the PC layer might help increase the water molecule coverage, bridging the performance gap between the liquid-and gas-phase water splitting systems. The temperature achieved at the SVG-PC interface may also play an important role in the high activity of our system.

Supplementary Discussion 4 | Elaboration on the techno-economic analysis of the floating photocatalyst sheet and particulate photocatalyst water splitting panel systems.

The techno-economic analysis of the hypothetical large-scale solar water splitting systems were based on the floating photocatalyst sheet design introduced in this study and on a previously reported particulate photocatalyst water splitting panel system.[3] The capital and operating costs of the large-scale systems were estimated assuming the general STH target for particulate photocatalytic system of 10%, capacity of 1 tonne per day of H_2, average solar insolation of 0.24 kW m^{-2}, and a facility lifetime of 20 years.[9–11]

The reactor subassemblies of both systems, consisting of a reaction chamber, an illumination window and support frames, are expected to be similar due to the fact that both systems comprise a photocatalyst immobilized on a sheet or panel[12] The costs of auxiliary equipment and control systems for gas handling, as well as the labour and energy required to operate them were estimated by extrapolating data from the economic analyzes of other solar H_2 production plants.[9,13,14] The land and maintenance costs of the two systems were taken as 6% of their equipment cost and total capital cost, respectively. The model particulate photocatalyst chosen for this techno-economic analysis was CoP-modified graphitic carbon nitride due to its scalability and high theoretical STH efficiency.[15–17] For the floating photocatalyst sheet system, the cost of the solar vapour generator was estimated from the current price of a commercially available carbon paper.

From the analysis (Supplementary Table 15), it can be seen that pure water is estimated to be one of the largest expenditures in a hypothetical large-scale solar water splitting system. Hence, the ability of the floating photocatalyst sheets to utilize contaminated water feedstocks for photocatalysis would significantly increase the economic feasibility of such a system. Operating the floating photocatalyst sheets over open bodies of water will further drive down the cost of this system by reducing the cost of land. In addition, this approach yield distilled water which can then be used by the neighbouring area for agriculture as well as consumption. However, it should be noted that the fabrication cost of the floating photocatalyst sheets is higher than the particulate photocatalyst water splitting panels due to the need for a solar vapour generator and a higher catalyst loading. This could be addressed by utilizing locally sourced carbonized biomass materials such as rice barn for the fabrication of the substrate for solar vapour generator.[18]

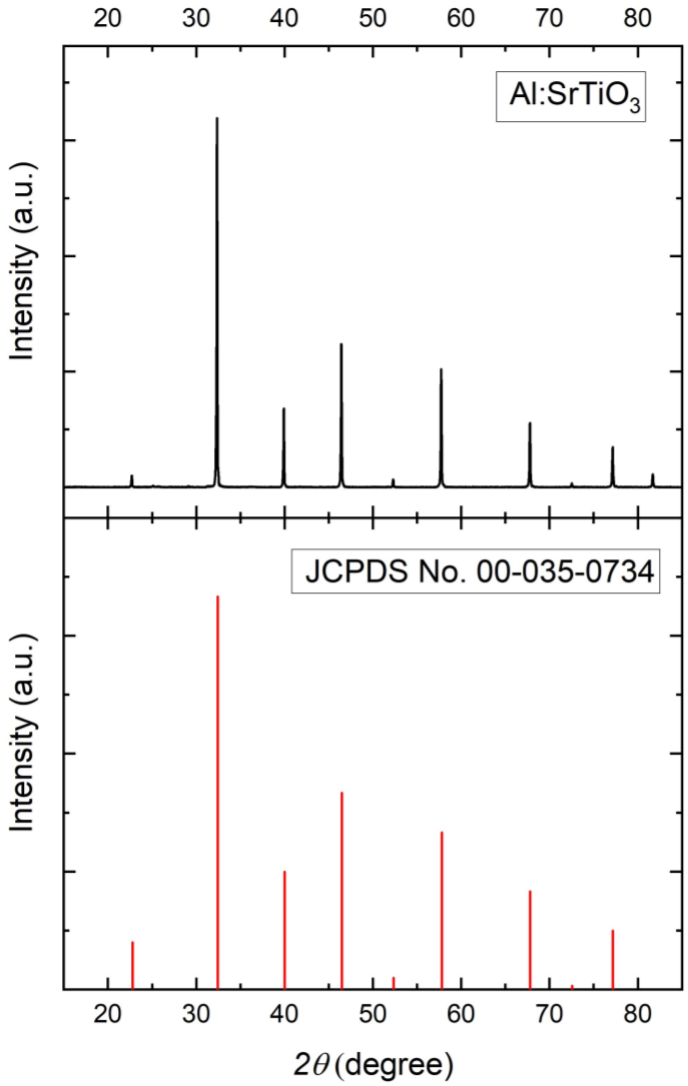

Supplementary Figure 1 | X-ray diffraction (XRD) patterns for Al:$SrTiO_3$. XRD peaks of Al:$SrTiO_3$ match with the standard pattern of $SrTiO_3$ (PDF No. 00-035-0734) and no other phases were found. XRD data processed using JADE software.

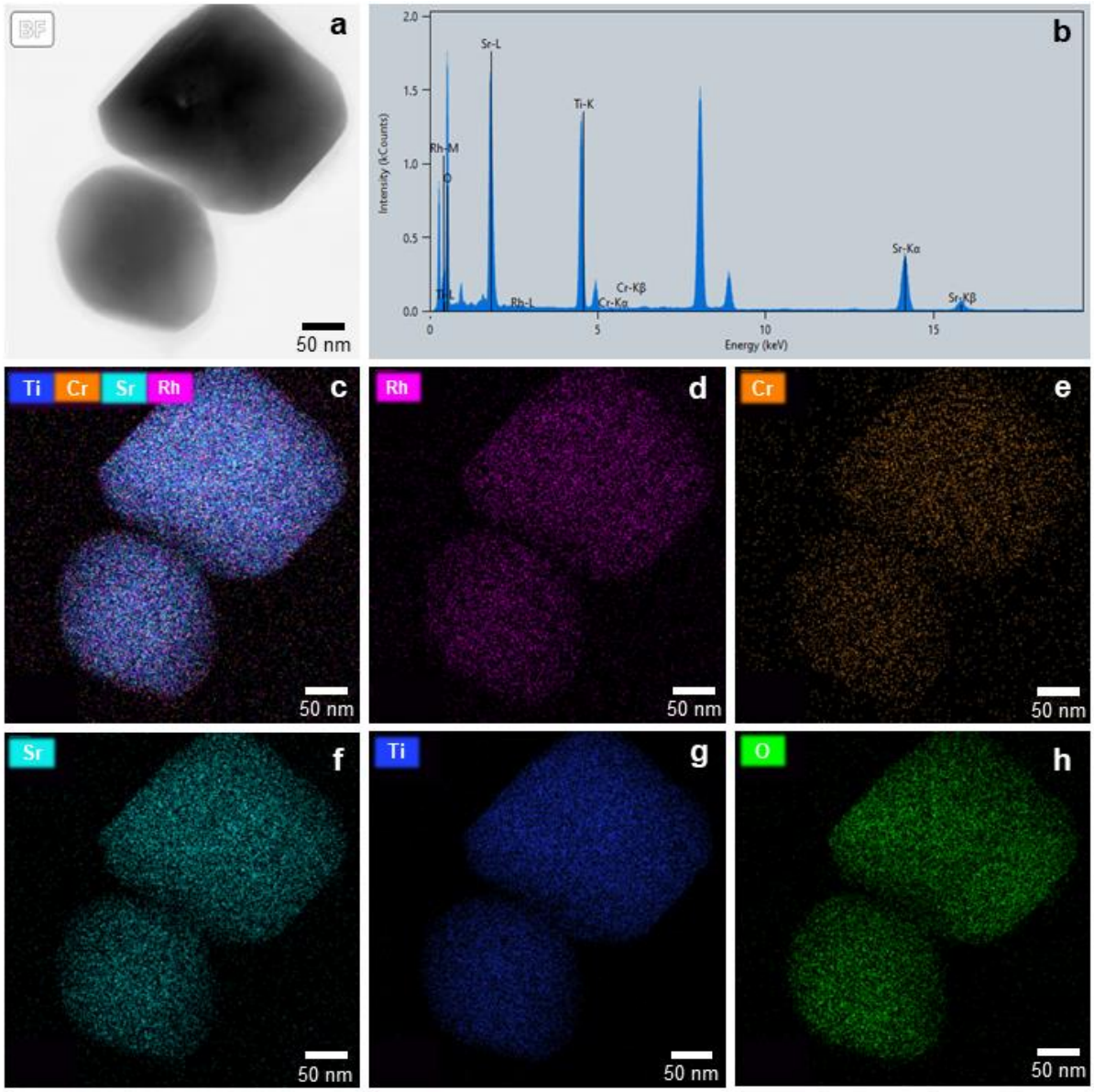

Supplementary Figure 2 | TEM images and energy-dispersive X-ray (EDX) elemental mapping of as-prepared $RhCrO_x$-Al:$SrTiO_3$ powder. a, TEM image of $RhCrO_x$-Al:$SrTiO_3$. **b,** EDX elemental spectrum corresponding to the area depicted in (**a**). **c-h,** Overall (**c**), Rh (**d**), Cr (**e**), Sr (**f**), Ti (**g**) and O (**h**) elemental mapping.

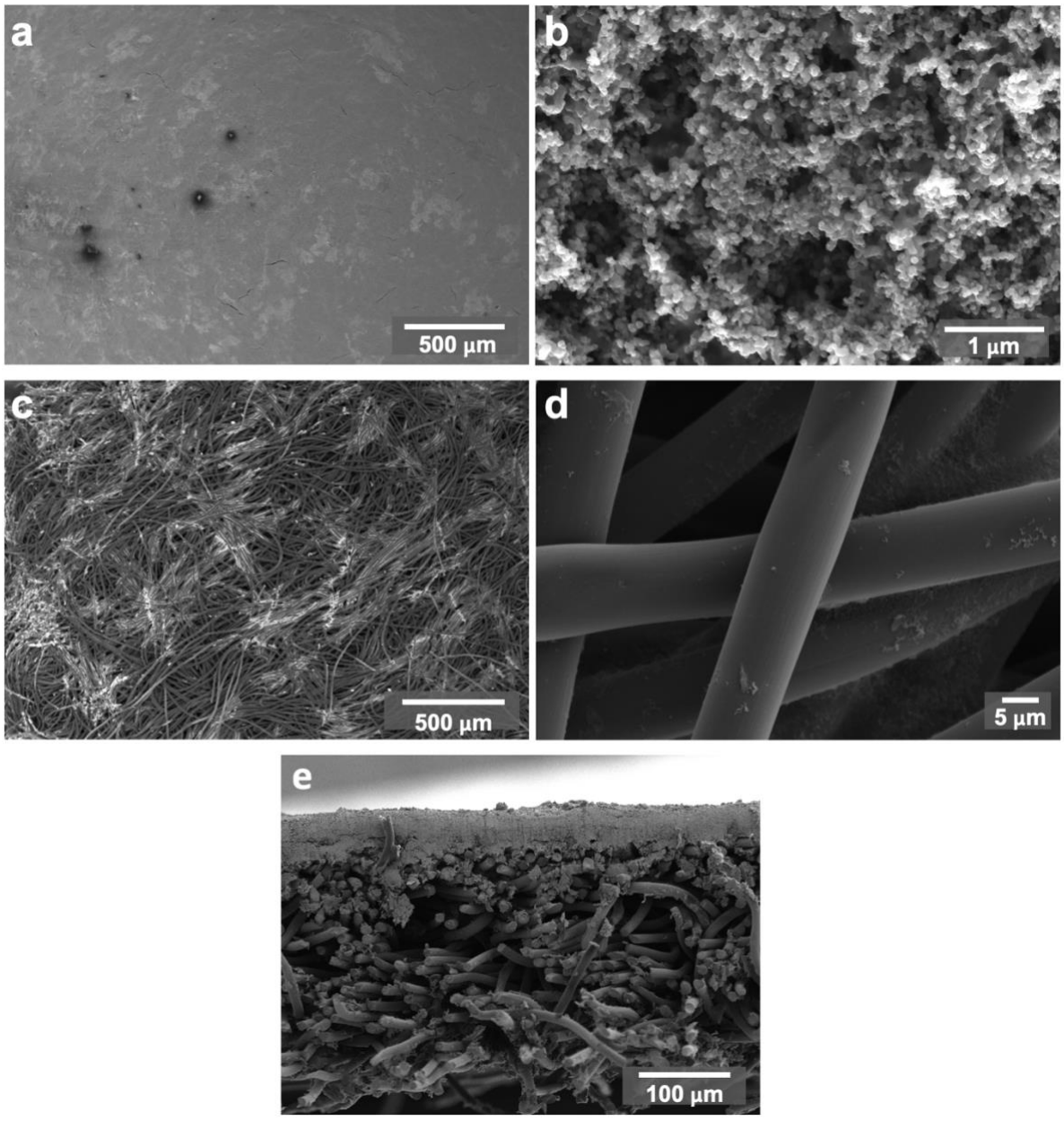

Supplementary Figure 3 | SEM images of the gas-diffusion carbon paper substrate which functions as an SVG. a, b, Top; **c, d,** bottom; and **e,** cross-sectional SEM images of the carbon paper. Mass per area of SVG is 0.012 g cm^{-2}.

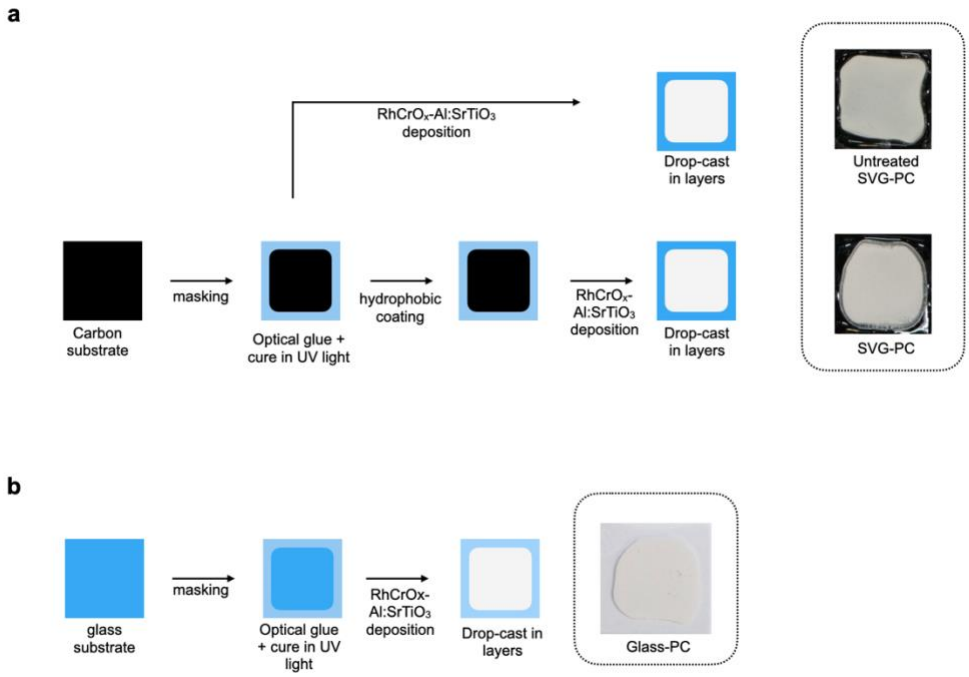

Supplementary Figure 4 | Step-by-step device assembly. a, Assembly of SVG-PC. The perimeter of a sheet of carbon paper is masked with optical glue and is hydrophobically-treated with DCDMS solution. Finally, $RhCrO_x$-Al:$SrTiO_3$ dispersed in IPA is drop-casted onto the sheet with a Nafion top-layer and dried at 338 K overnight. In the case of untreated SVG-PC, the hydrophobic treatment is skipped. **b,** Assembly of Glass-PC. The perimeter of a glass sheet is masked with optical glue. $RhCrO_x$-Al:$SrTiO_3$ dispersed in IPA is drop-casted onto the sheet. The glue mask was removed and the sheet was annealed at 573K for 1 h.

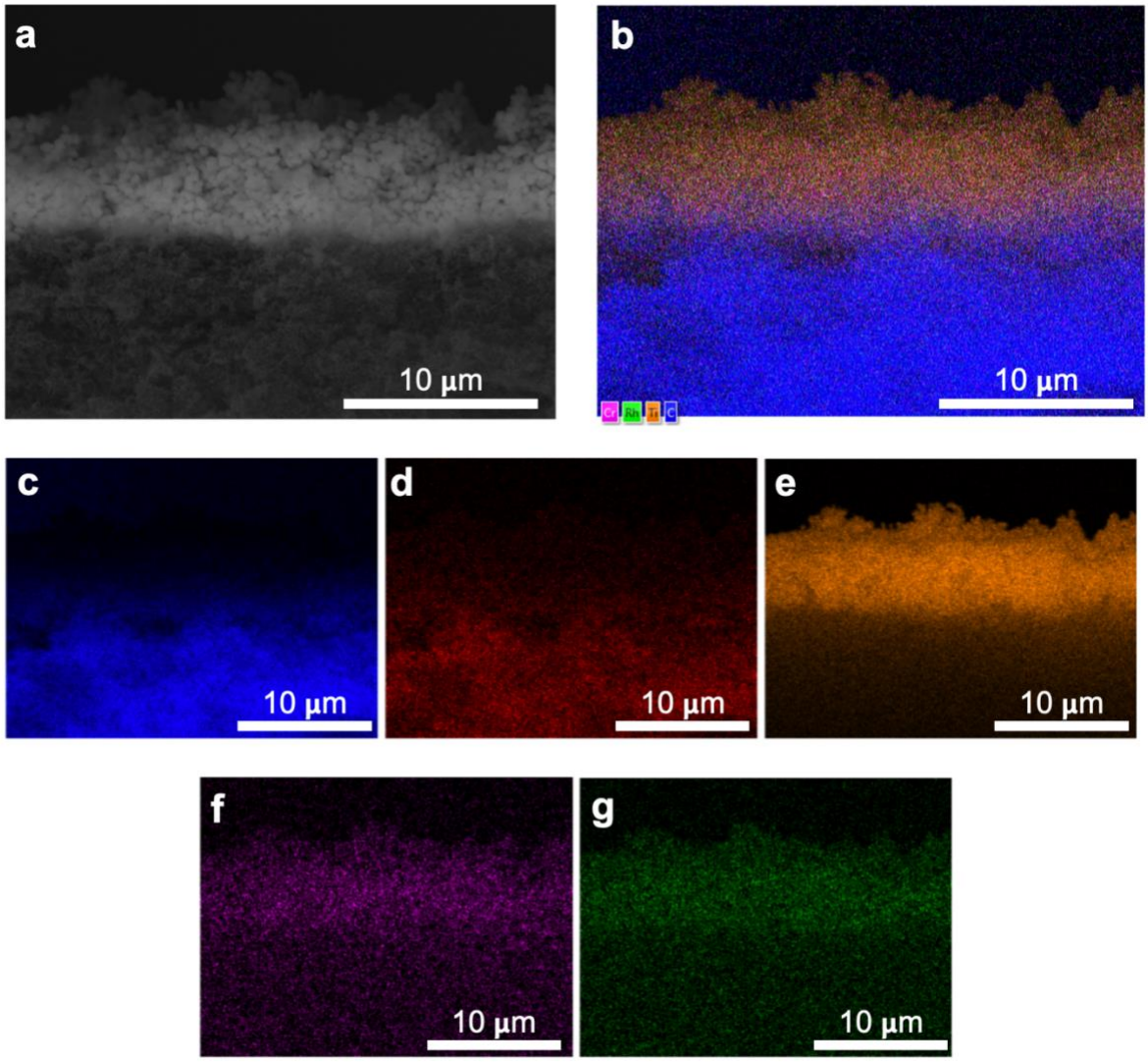

Supplementary Figure 5 | Cross-section SEM images and energy-dispersive X-ray (EDX) elemental mapping of as-prepared SVG-PC sheet. a, SEM image recorded at 15.0 kV beam intensity. **b-g**, Overall (**b**), carbon (**c**), fluorine (**d**), titanium (**e**), chromium (**f**) and rhodium (**g**) elemental mapping.

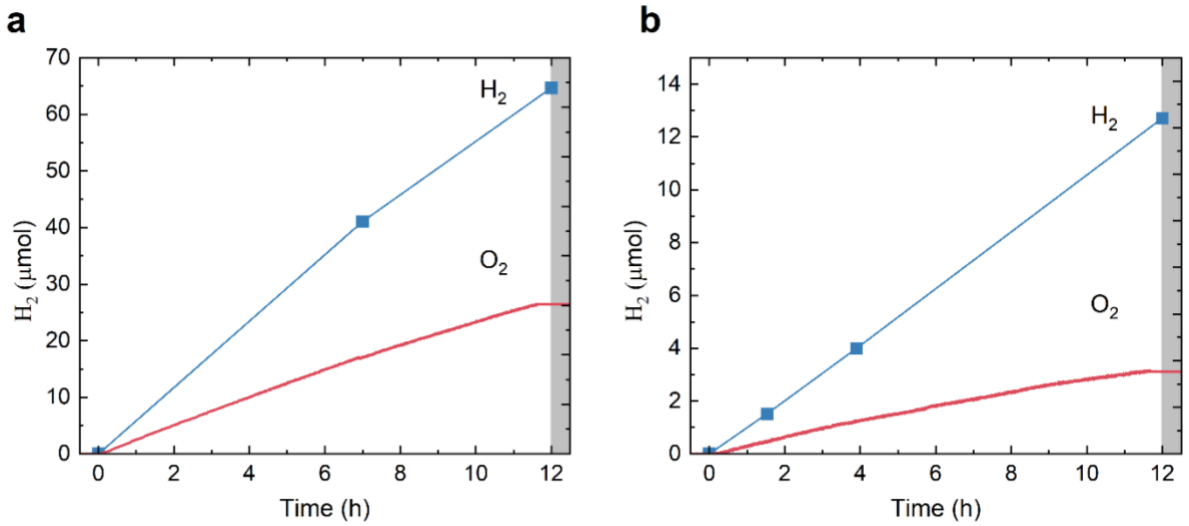

Supplementary Figure 6 | A typical time course of the water-splitting reaction over a $RhCrO_x$-Al:$SrTiO_3$ photocatalyst. a, **b**, $RhCrO_x$-Al:$SrTiO_3$ suspension in distilled water (**a**) and in artificial seawater (**b**). Photocatalytic measurements were performed under simulated sunlight (AM 1.5G, 100 mW cm^{-2}). The grey portion of the graphs indicate when the samples were removed from irradiation, allowing the baseline O_2 to be measured to account for possible O_2 leakage.

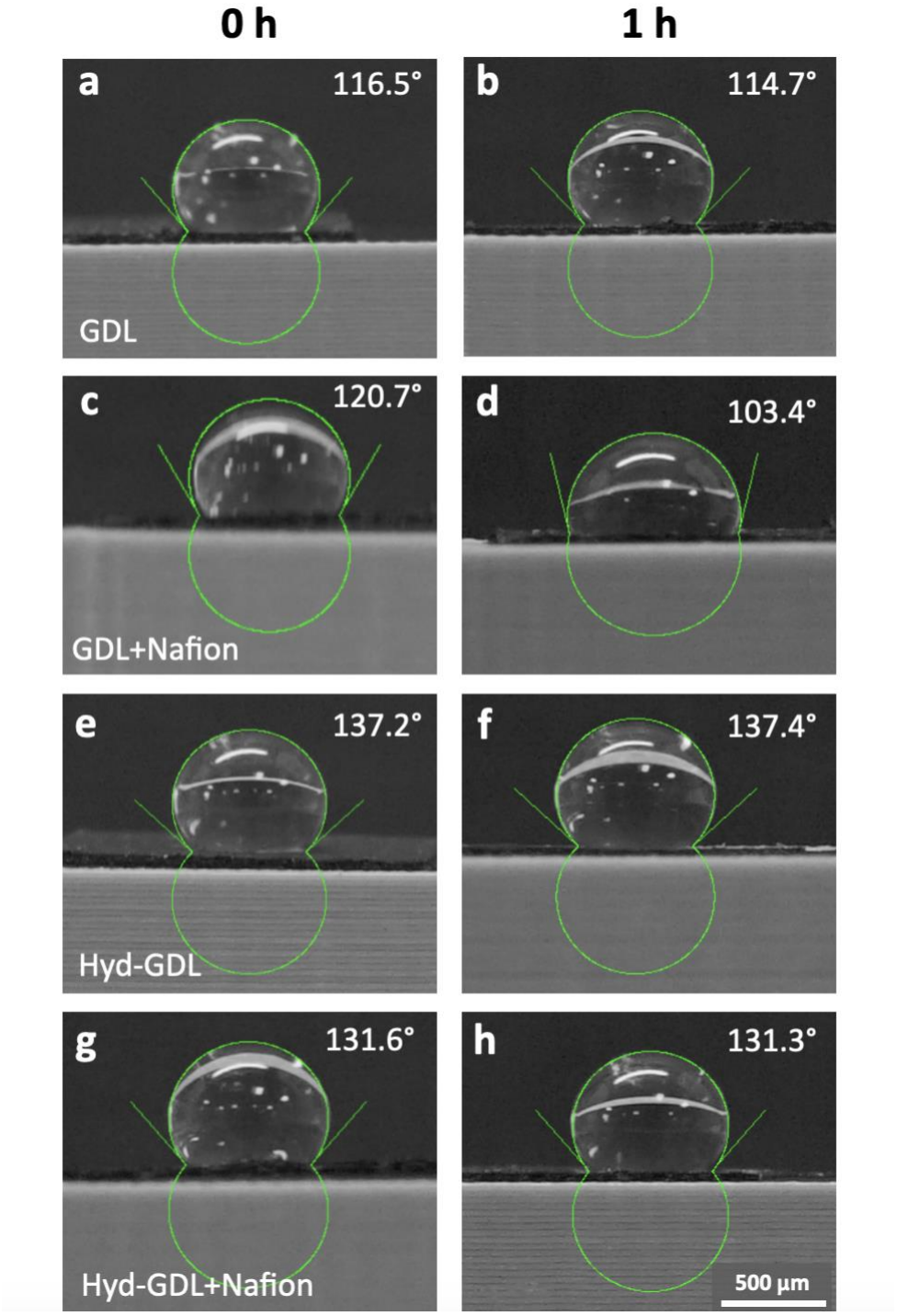

Supplementary Figure 7 | Contact angle measurement of SVG. a, **b**, Contact angle of SVG at 0 h (**a**) and 1 h (**b**). **c**, **d**, Contact angle of Nafion-coated SVG at 0 h (**c**) and 1 h (**d**). **e**, **f**, Contact angle of hydrophobically-treated SVG at 0 h (**e**) and 1 h (**f**). **g**, **h**, Contact angle of Nafion-coated on hydrophobically-treated SVG at 0 h (**g**) and 1 h (**h**). To carry out the contact angle measurements, two sets of sheets were floated on pure water; a droplet of water was applied to the first set at 0 h and the second set at 1 h.

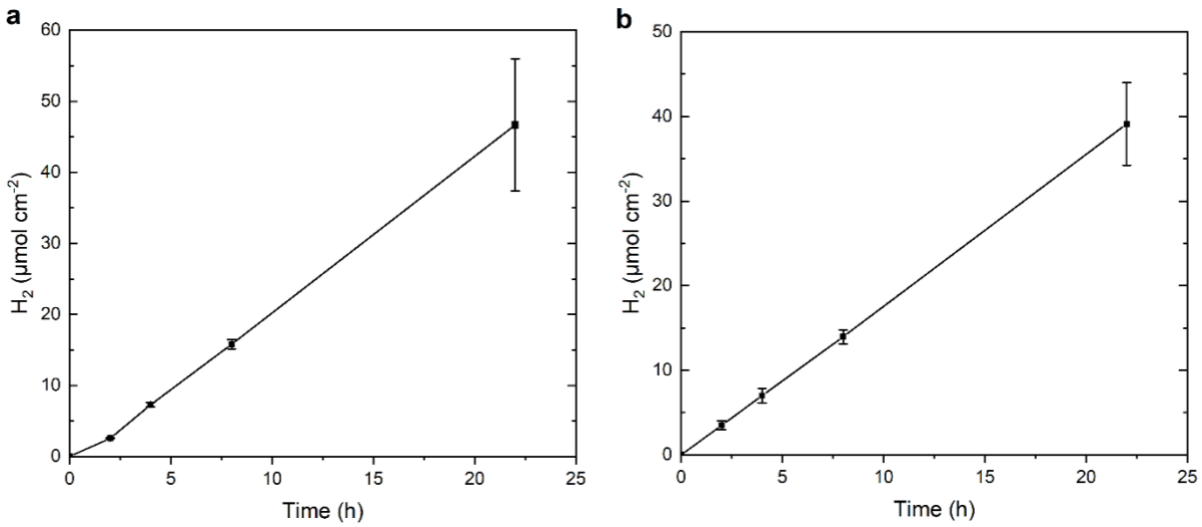

Supplementary Figure 8 | Sample time course of H_2 evolution using SVG-PC. a-b. H_2 evolution measurements performed over pure water (**a**) and seawater (**b**). Conditions: 2.0 mg $RhCrO_x$-Al:$SrTiO_3$ deposited on hydrophobic-treated SVG, irradiation (AM 1.5G, 1 sun, 22 h). Data are presented as mean values ± SD with n = 3.

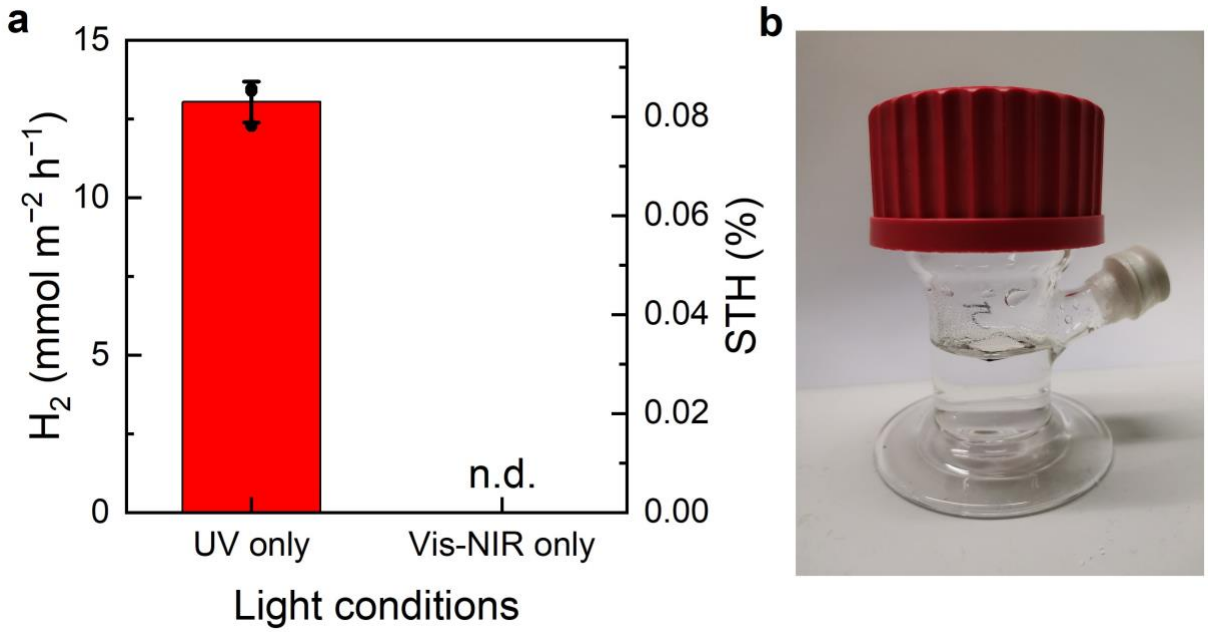

Supplementary Figure 9 | Photocatalytic experiments conducted under different light conditions. (**a**) H_2 evolution rate of SVG-PC under UV and Vis-NIR light. (**b**) Photograph of the photoreactor taken after conducting the photocatalytic experiment under only UV irradiation. Condensation on the walls of the photoreactor indicate that water vapour builds-up in the reactor despite the exclusion of Vis and NIR light. Photocatalytic measurements were performed over pure water for 22h. n.d. – not detected. Reported value can be seen in Supplementary Table 7. Data are presented as mean values ± SD with n = 3.

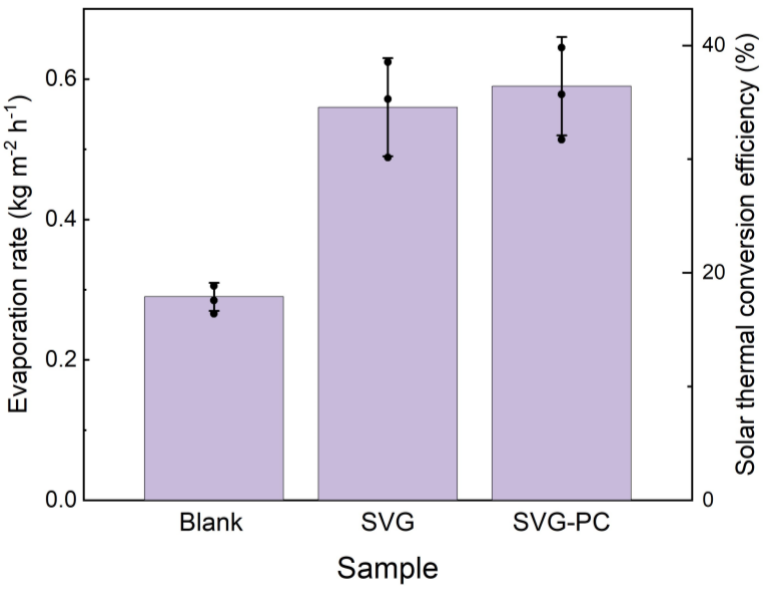

Supplementary Figure 10 | Solar vapour generation rate for the photothermal-photocatalyst sheets and SVG substrate under UV light irradiation. Water evaporation measurements were performed using pure water for 4 h, respectively. Data are presented as mean values ± SD with n = 3.

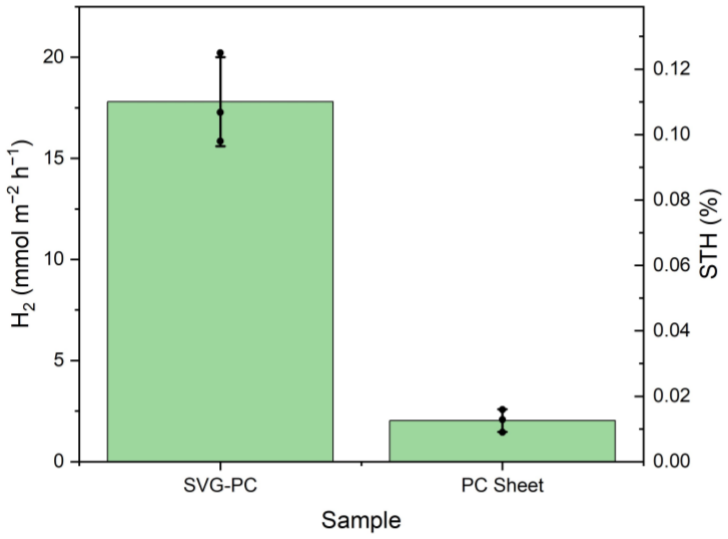

Supplementary Figure 11 | H_2 evolution of SVG-PC floating directly on and suspended over seawater. SVG-PC was not in contact with the liquid phase in the latter case. Photocatalytic experiments were performed under AM 1.5G, 22 h at room temperature. Data are presented as mean values ± SD with n = 3.

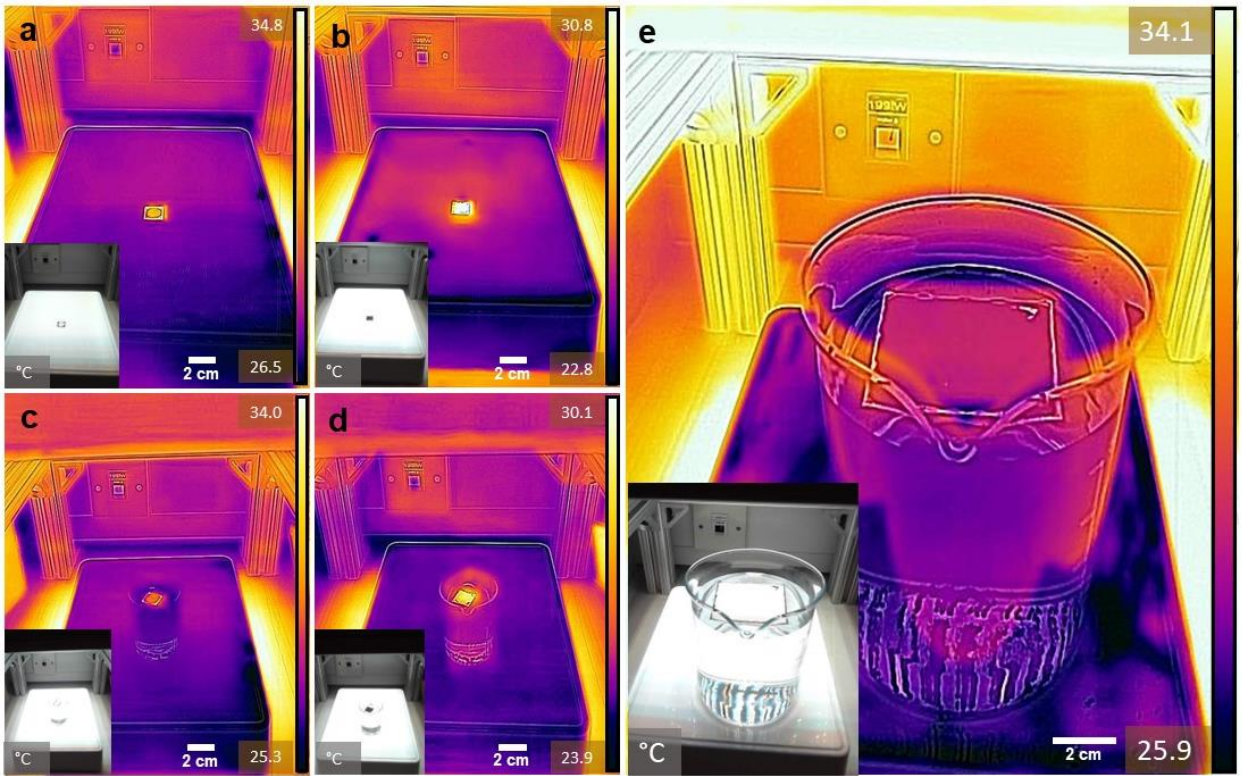

Supplementary Figure 12 | Infrared thermal images of SVG-PC and SVG under 1 sun irradiation. a, **b**, Thermal image of SVG-PC (**a**) and SVG (**b**) in air. **c, d,** Thermal image of SVG-PC (**c**) and SVG (**d**) over water. **e,** Thermal image of 25 cm^2 SVG-PC over water. The insets show the corresponding optical image of each sample. Bar on right of the infrared thermal images represents temperatures.

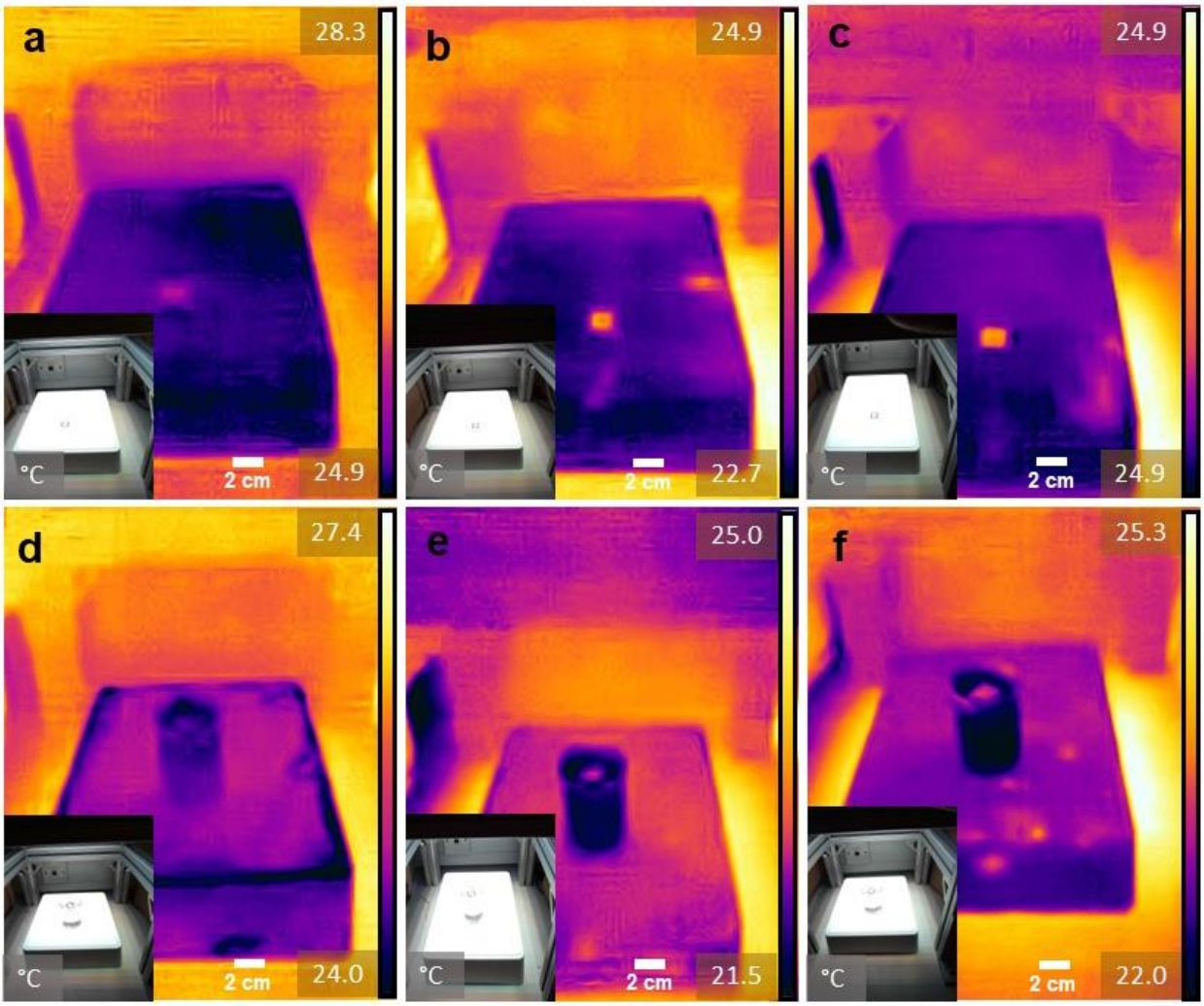

Supplementary Figure 13 | Infrared thermal images of SVG-PC under 0.2-0.7 sun irradiation. a-c, Thermal image of SVG-PC in air under 0.2 (**a**), 0.5 (**b**) and 0.7 (**c**) sun irradiation. **d-f,** Thermal image of SVG-PC floating on the surface of water under 0.2 (**d**), 0.5 (**e**) and 0.7 (**f**) sun irradiation. The insets show the corresponding optical image of each sample. Bar on right of the infrared thermal images represents temperatures.

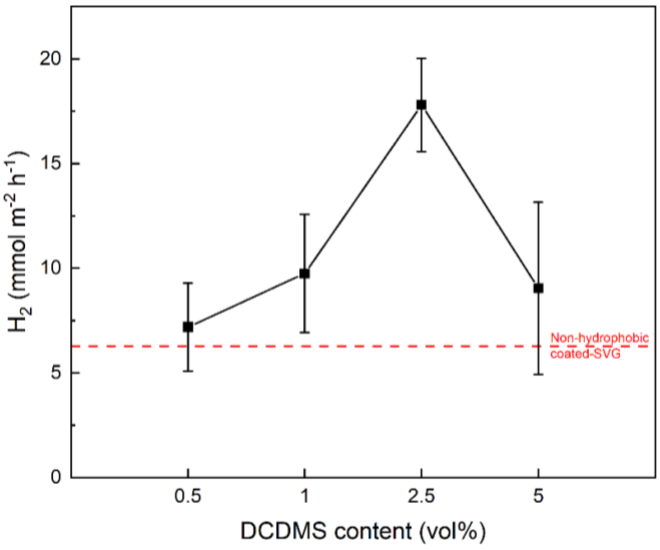

Supplementary Figure 14 | H_2 evolution rate of SVG-PC fabricated on hydrophobically-treated SVG with various DCDMS concentration. An optimum DCDMS concentration is 2.5 vol% DCDMS**.** Increasing the concentration of DCDMS to 5 vol% results in two times lower H_2 evolution rate compared to 2.5 vol% DCDMS. Reported value can be seen in Supplementary Table 17. Data are presented as mean values ± SD with n = 3.

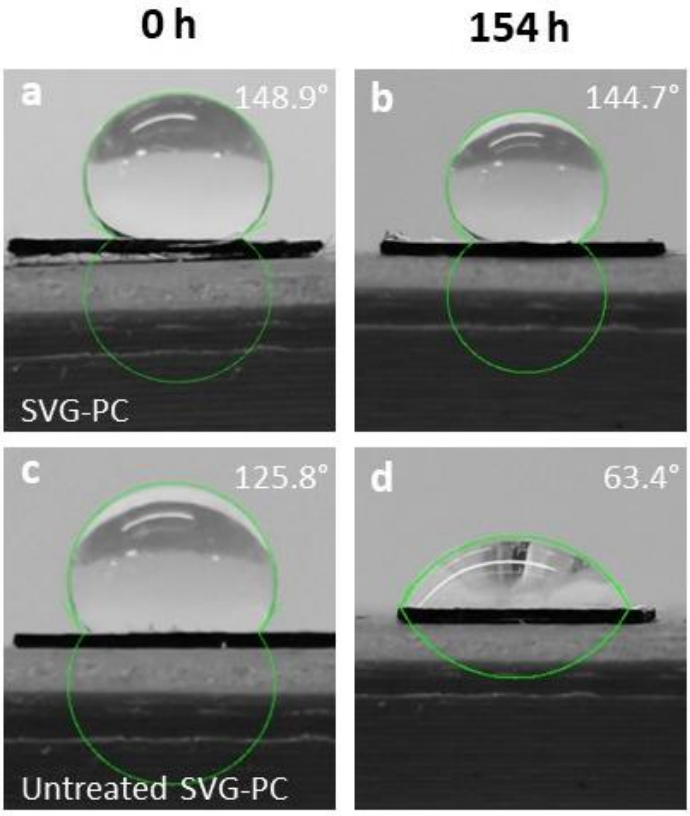

Supplementary Figure 15 | Contact angle measurement of photocatalyst sheets. a, b, Contact angle of SVG-PC at 0 h (**a**) and 154 h (**b**). **c, d,** Contact angle of untreated SVG-PC at 0 h (**c**) and 154 h (**d**).

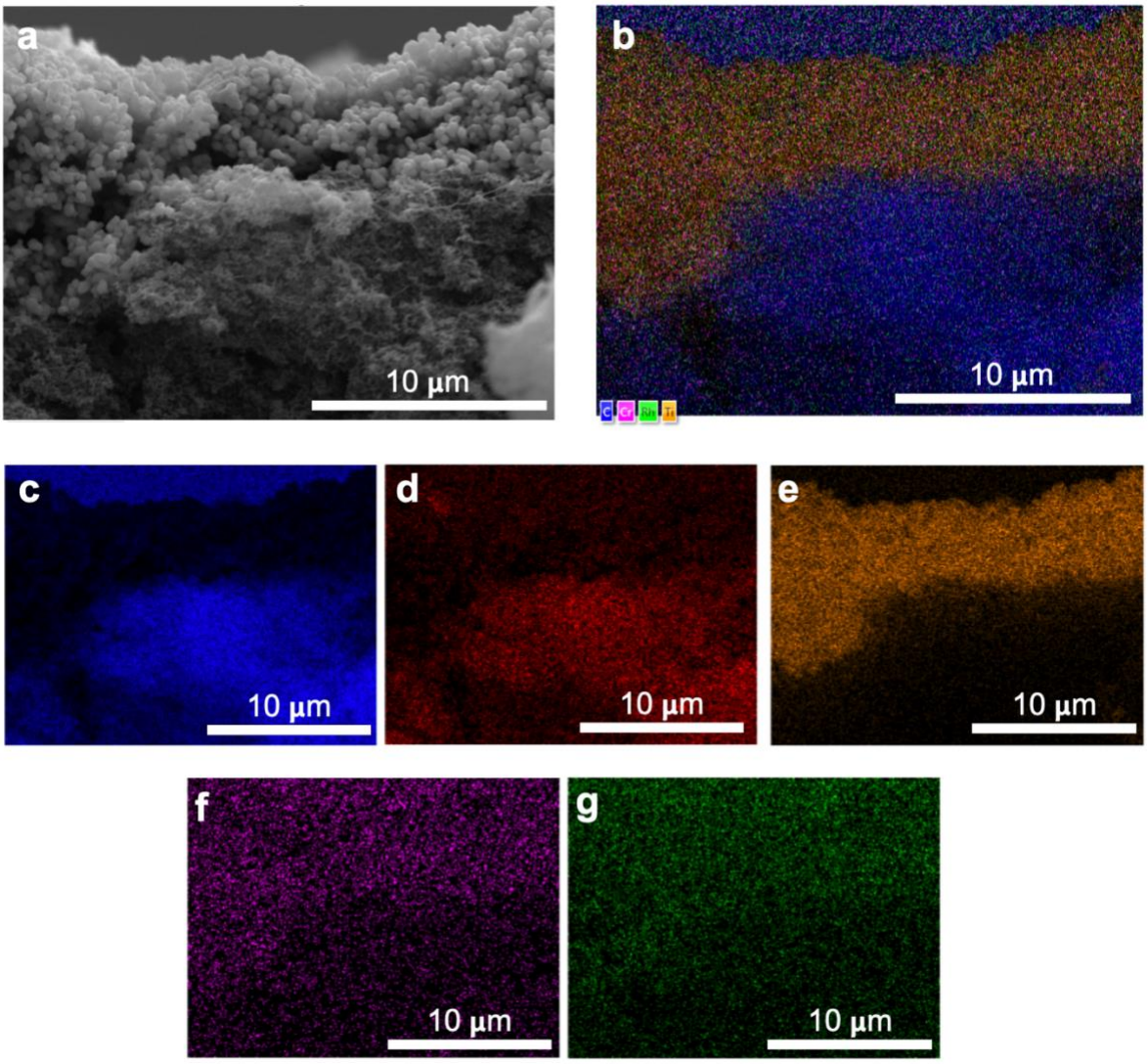

Supplementary Figure 16 | Cross-section SEM images and energy-dispersive X-ray (EDX) elemental mapping of SVG-PC sheet after 150 h operation under 1 sun irradiation. a, SEM image recorded at 15.0 kV beam intensity. **b-g**, Overall (**b**), carbon (**c**), fluorine (**d**), titanium (**e**), chromium (**f**) and rhodium (**g**) elemental mapping.

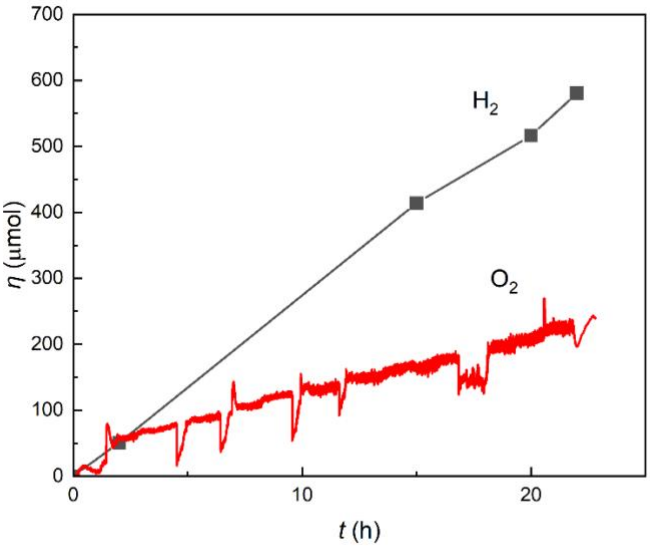

Supplementary Figure 17 | Time course of H_2 and O_2 evolution via the water splitting reaction using 25 cm^2 SVG-PC over artificial seawater. Photocatalytic measurements were performed under simulated sunlight (AM 1.5G, 100 mW cm^{-2}). Fluctuations in the O_2 measurements were likely due to the formation of water droplets on the oxygen sensor probe via condensation.

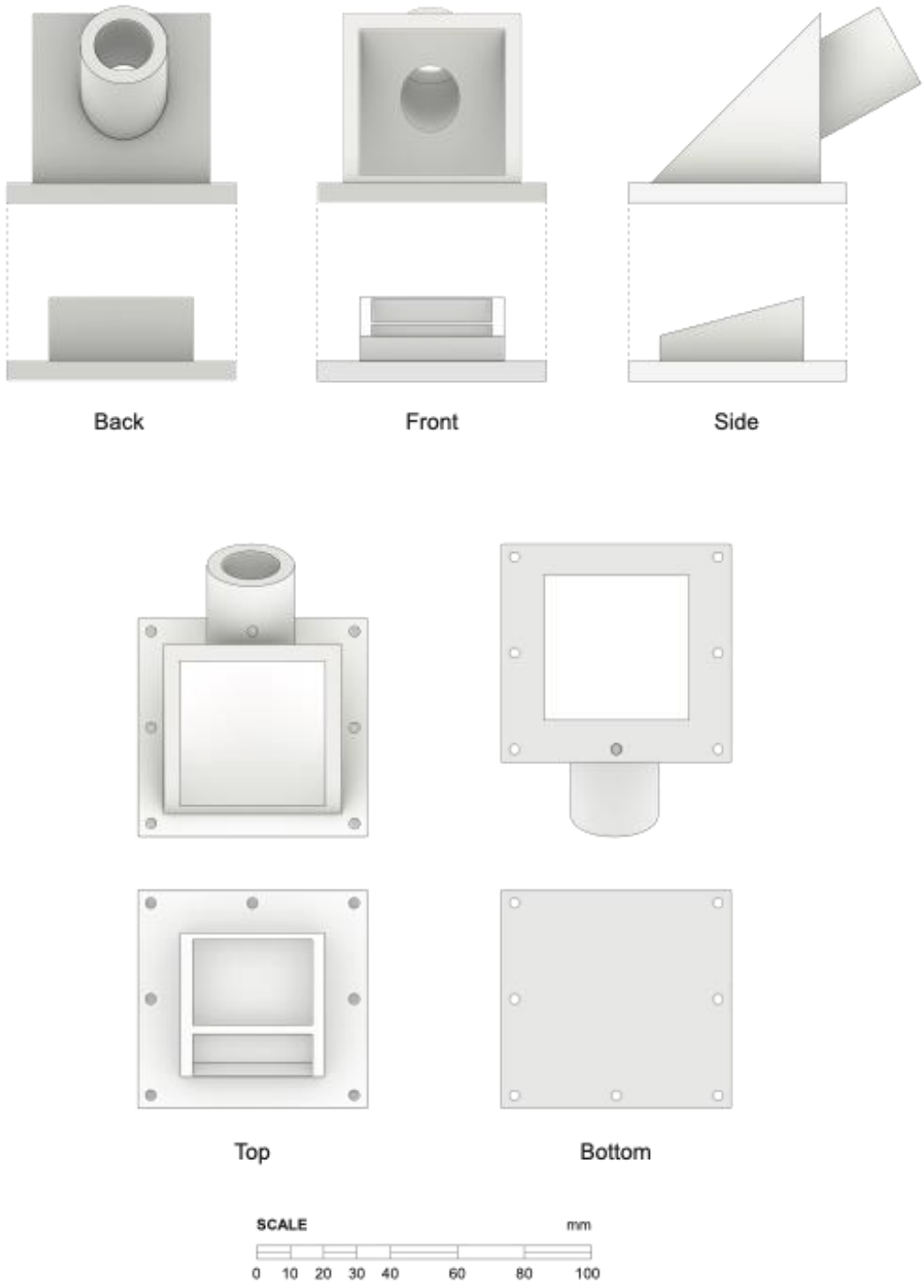

Supplementary Figure 18 | Sketches of the custom reactor used to demonstrate integrated water splitting and clean water production by hybrid photothermal-photocatalyst sheets and its components. Diagram shows 2D projections of top, bottom and side views of the photoreactor.

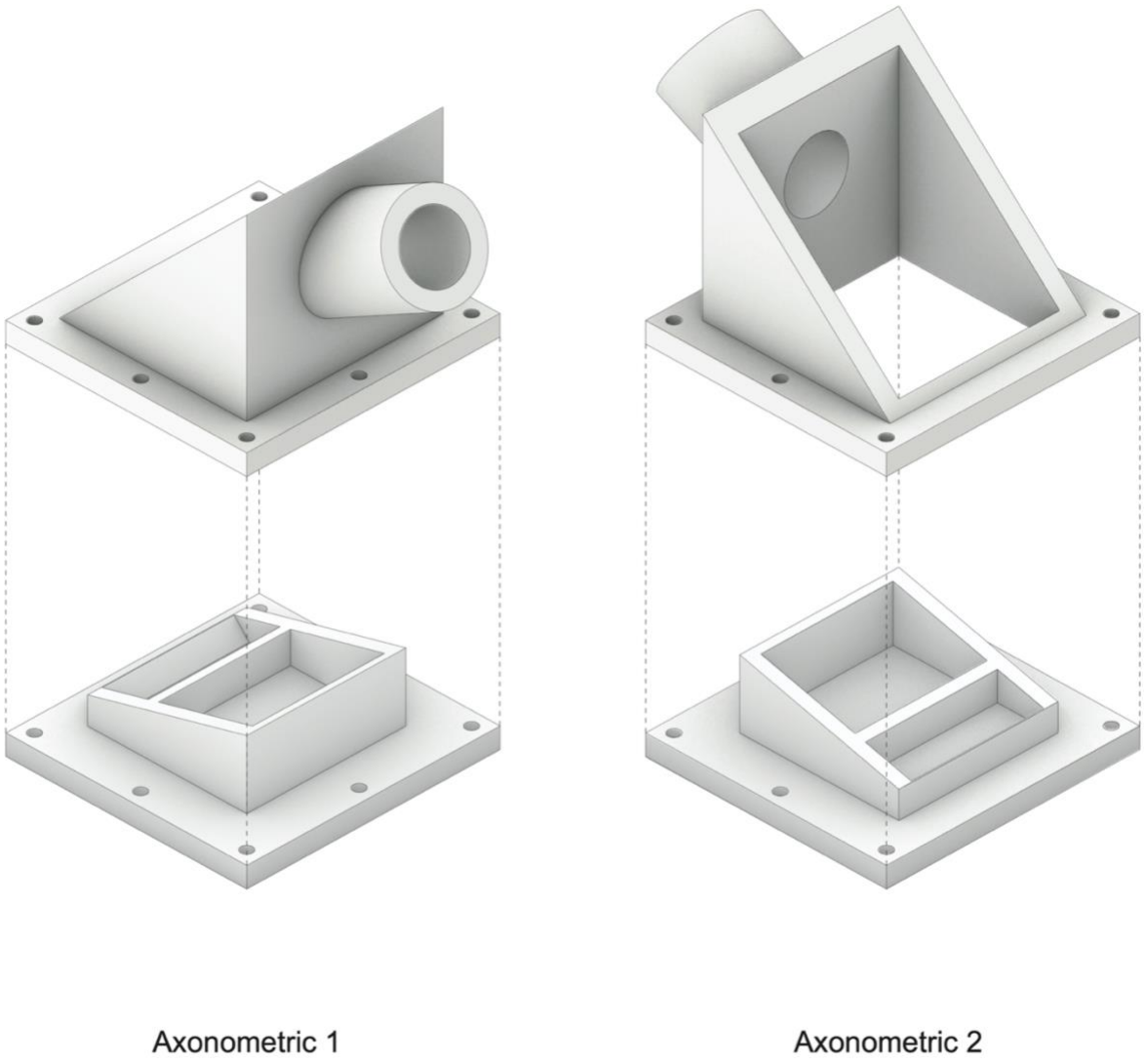

Supplementary Figure 19 | Schematic diagram showing axonometric views of the photoreactor used to demonstrate integrated water splitting and clean water production by hybrid photothermal-photocatalyst sheets. The 3D-printed reactor was printed using CPE+ (co-polyester) filament. UV-transmitting Plexiglass was attached to the top part of the cell using two-part epoxy.

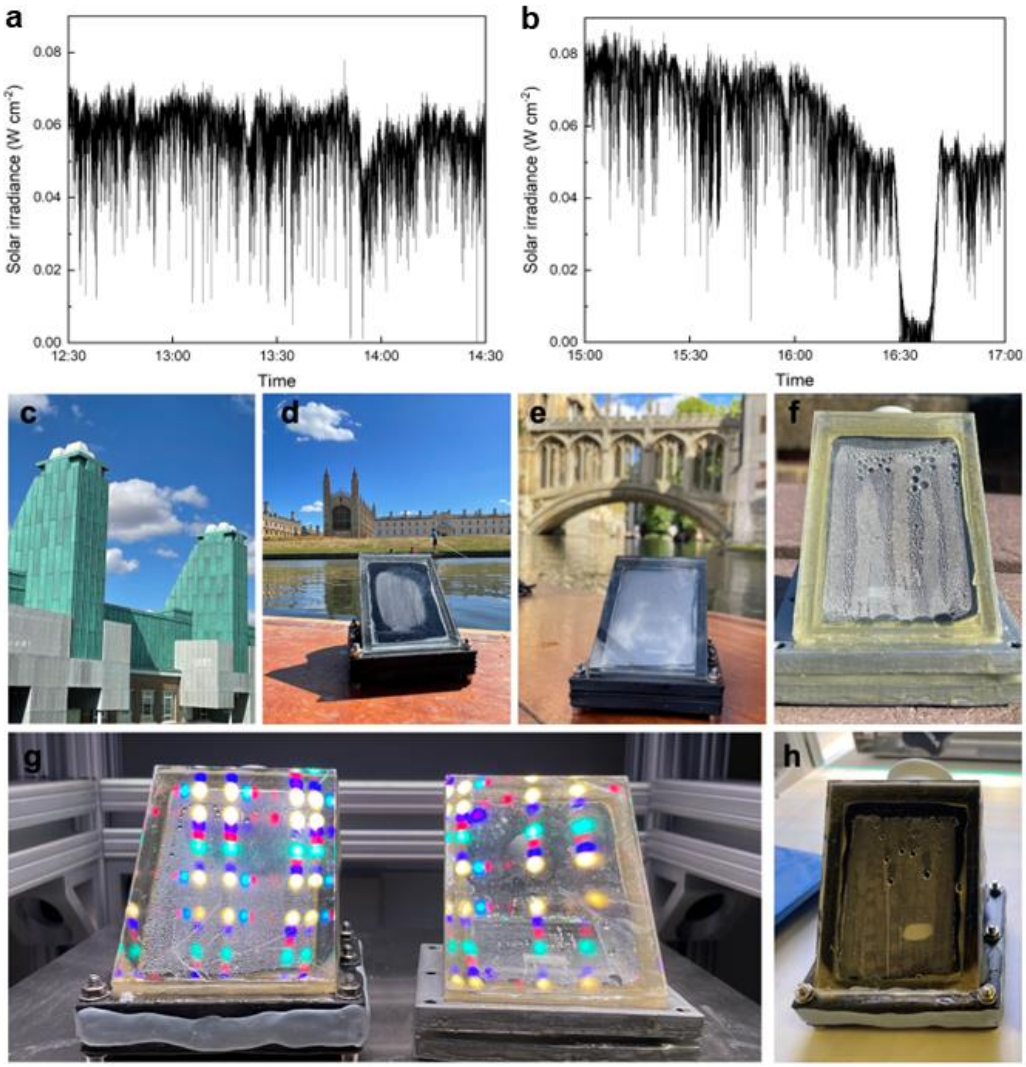

Supplementary Figure 20 | Integrated H_2 and clean water production by SVG-PC under simulated and natural sunlight using water from river Cam. a, Light intensity during a 2 h test on the 6th of August 2022, between 12:30 – 14:30 (sunny, corresponding to approximately 0.6 sun, T ≈ 21°C). **b**, Light intensity during a 2 h test on the 6th of August 2022, between 15:00 – 17:00 (mostly sunny with a period of overcast, corresponding to approximately 0.7 sun, T ≈ 24°C). **c**, Sloped roof of the Yusuf Hamied Department of Chemistry building as inspiration for the design of the photoreactor for integrated water splitting and clean water production. **d**, **e**, Photograph of the photoreactor along the River Cam in front of King's College Chapel (**d**) and the Bridge of Sighs, St John's College (**e**). **f**, A closeup photo of the reactor showing condensed water droplet formed on the front window of the reactor during outdoor experiment. **g**, Indoor test conducted using a G2V Sunbrick LED Solar Simulator calibrated to match AM 1.5G irradiation. The coloured reflections correspond to the different-wavelength LEDs which are amassed to produce the AM 1.5G spectrum. **h**, Photograph of the photoreactor after conducting the photocatalytic experiment under simulated sunlight. H_2 is trapped in the gas-tight headspace of the photoreactor while water vapour produced by the SVG condenses on the sloped window and accumulates to form larger droplets which then flow into a separate partition for collection.

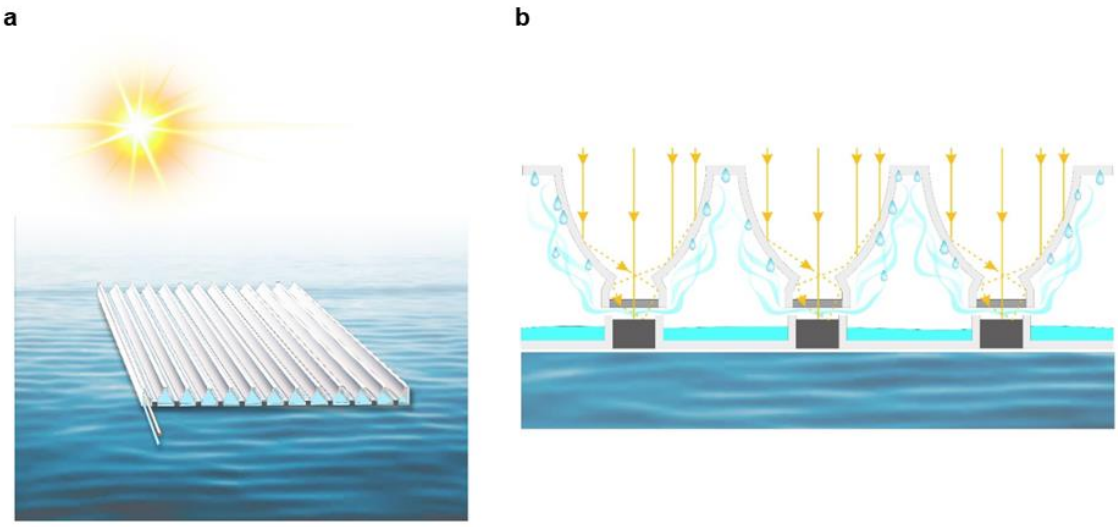

Supplementary Figure 21 | Proposed design of a reactor for large-scale application of the floating photocatalyst sheets with solar concentration. a, 3D rendering and **b,** side-view of the reactor. The reactor can float on the surface of a body of water, such as the sea. Parabolic mirrors will concentrate sunlight onto the photocatalyst sheets. The produced water will be trapped in the reactor compartments and can be subsequently collected. The hydrogen and oxygen produced would be circulated away from the reactor headspace to reduce overpressure. The gas mixture can be transported to an on-shore gas separation unit. Gas separation could then be done via conventional membrane separation. The SVG-PC device in our proposed reactor makes a direct contact with the water supply (such as seawater and waste streams), thus omitting the need for an extra water supply and a desalination mechanism.

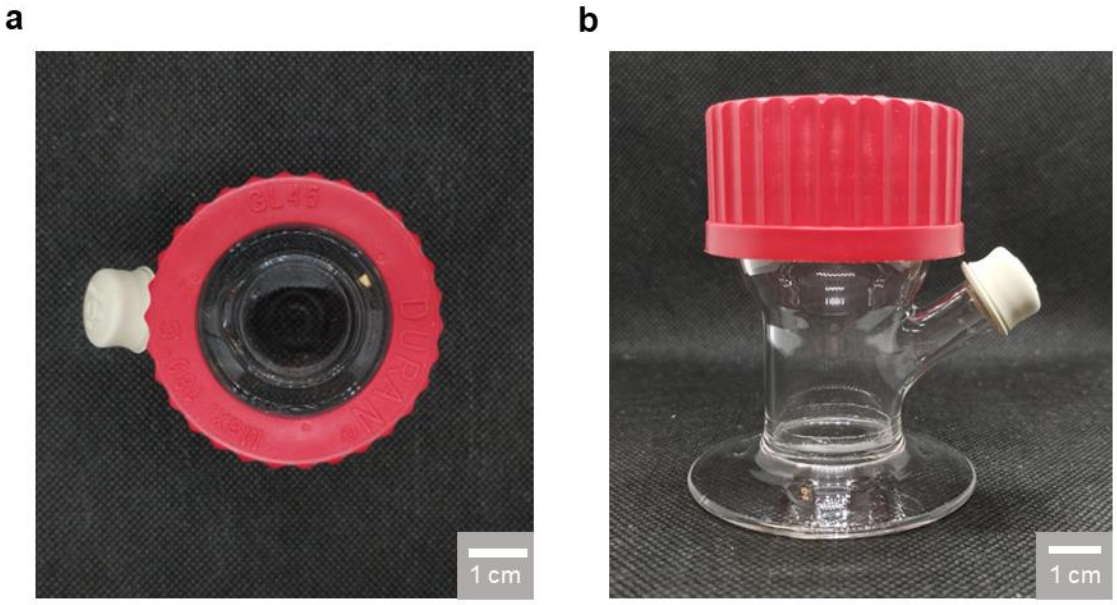

Supplementary Figure 22 | Photographs of top-irradiation-type glass photoreactor used for photocatalytic reaction. Photograph of the reactor from the top view (a) and side view (b). The optical transparent quartz window is used to allow full solar irradiation to reach the device.

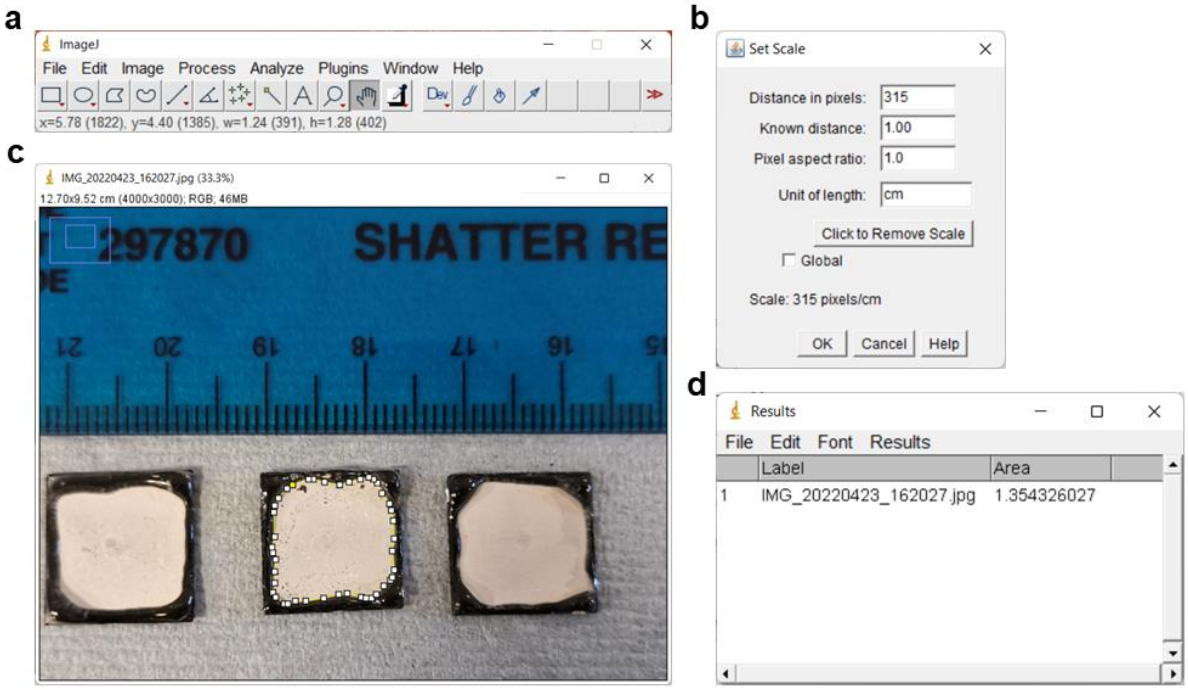

Supplementary Figure 23 | Measurement of the photocatalyst sheet photoactive area using the ImageJ software. a, ImageJ user interface. **b**, Calibration of the measurement tool by setting the conversion ratio of number of pixels in photograph to actual length. **c,** Highlighting the parameter of the active area of the photocatalyst sheet. **d**, Output from the software gives the area of the highlighted region.

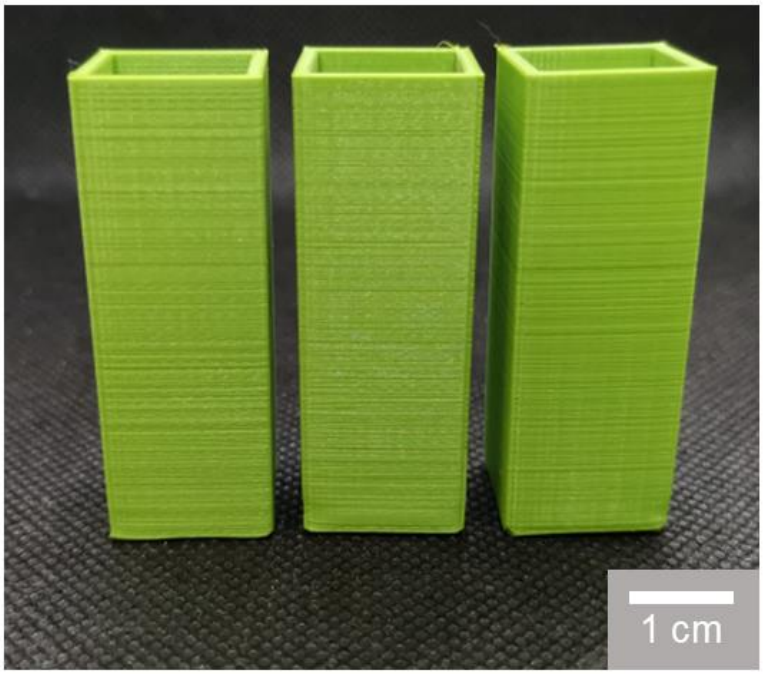

Supplementary Figure 24 | Photographs of the custom-designed photoreactors for solar vapour characterization. 3D-printed reactor with a dimension of 1.5 × 1.5 × 5.0 cm^3. The reactors were printed using polylactic acid (PLA) filament.

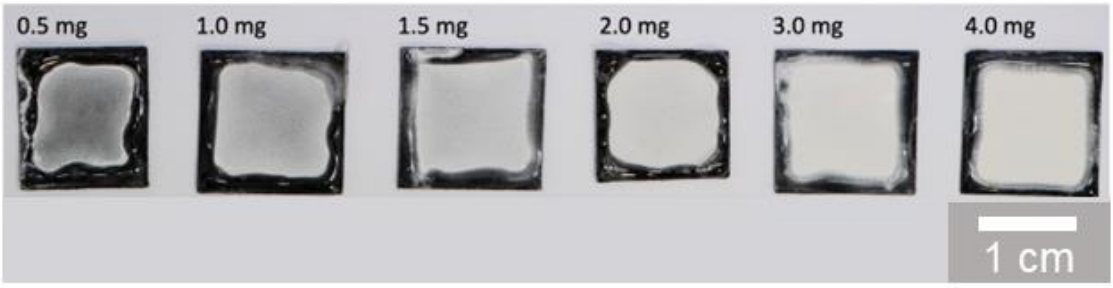

Supplementary Figure 25 | Photographs of SVG-PC at different $RhCrO_x$-Al:$SrTiO_3$ loading.

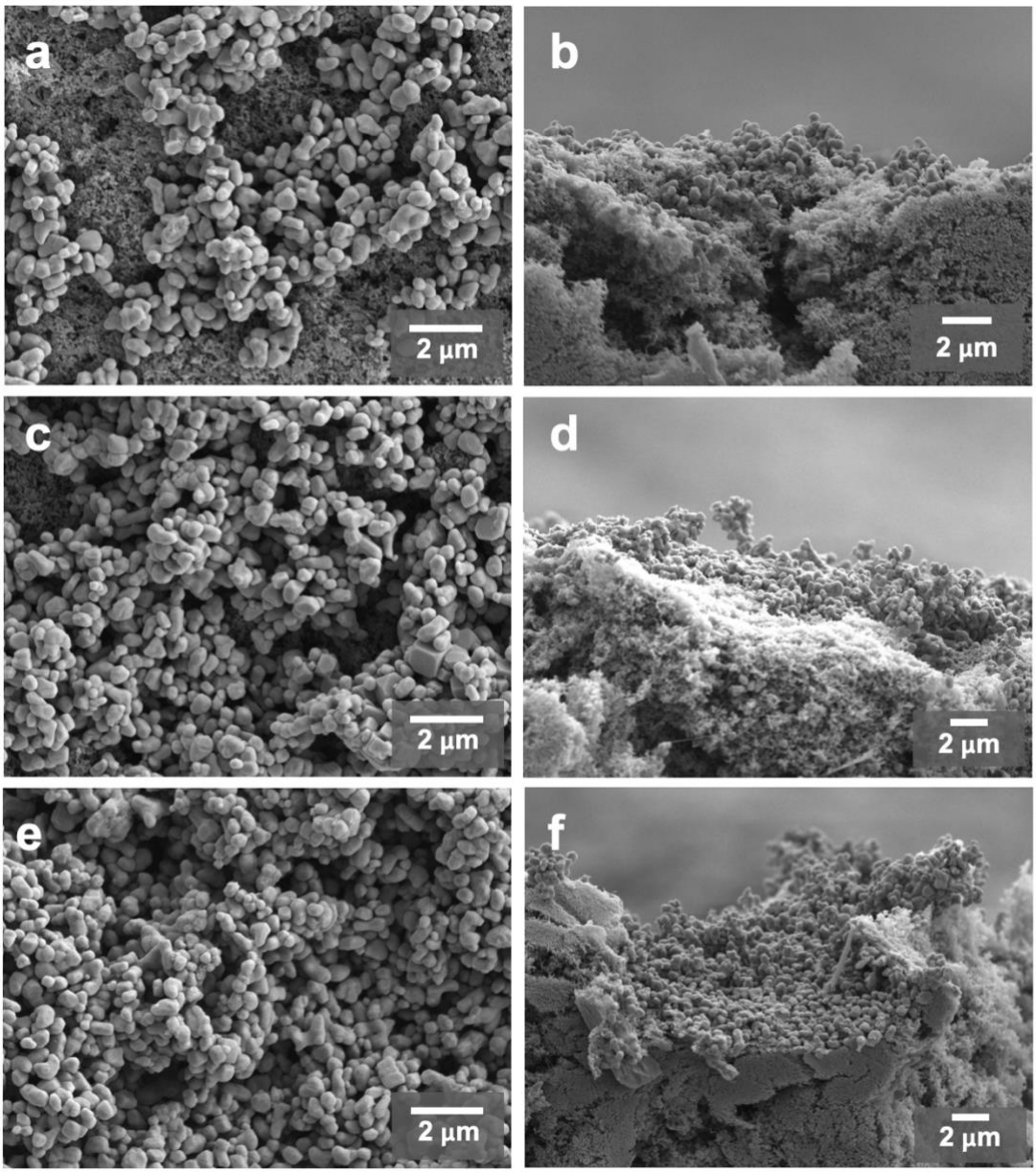

Supplementary Figure 26 | SEM images of SVG-PC at different $RhCrO_x$-Al:$SrTiO_3$ loading. a, **b,** 0.5 mg cm^{-2} -loaded SVG-PC sheet. **c**, **d,** 1.0 mg cm^{-2} -loaded SVG-PC sheet. **e**, **f,** 1.5 mg cm^{-2} -loaded SVG-PC sheet. **a**,**c**,**e**, Top views. **b**,**d**,**f**, Cross-section SEM images.

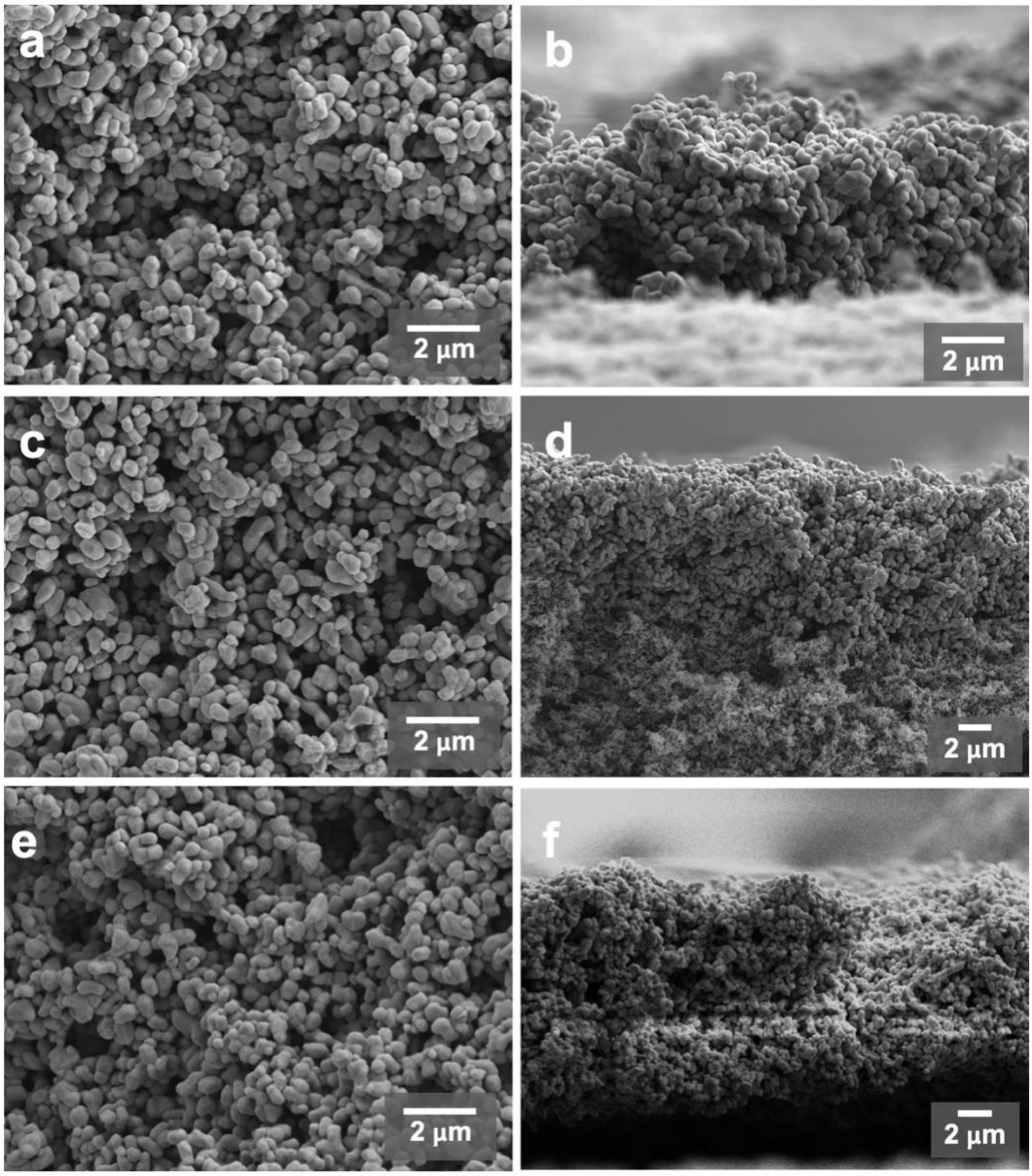

Supplementary Figure 27 | SEM images of SVG-PC at different $RhCrO_x$-Al:$SrTiO_3$ loading. a, **b**, Top-view (**a**) and Cross-section SEM image (**b**) of 2.0 mg cm^{-2}-loaded SVG-PC sheet. **c**, **d**, Top-view (**a**) and Cross-section SEM image (**b**) of 3.0 cm^{-2} -loaded SVG-PC sheet. **e**, **f**, Top-view (**e**) and Cross-section SEM image (**f**) of 4.0 mg cm^{-2}-loaded SVG-PC sheet.

Supplementary Table 1 | ICP-OES analysis of the Rh and Cr content of photocatalyst sheets before and after 154 h of irradiation. The photocatalysis experiments were carried out under AM 1.5G.

Sample	Element content (ppm)		Cr/Rh ratio
	Rh	Cr	
Fresh samples			
$RhCrO_x$-Al:$SrTiO_3$ powder	0.816	0.901	1.10
SVG-PC	0.289	0.425	1.47
Samples after 154 h of operation			
Glass-PC in H_2O	0.51	0.323	0.63
Glass-PC in Seawater	0.255	0.221	0.87
Untreated SVG-PC in H_2O	0.408	0.255	0.63
Untreated SVG-PC in Seawater	0.153	0.238	0.66
SVG-PC-H_2O	0.476	0.612	1.29
SVG-PC-Seawater	0.323	0.493	1.53

Supplementary Table 2 | Water evaporation rate of SVG-PC with different $RhCrO_x$-Al:$SrTiO_3$ loading. Conditions: irradiation (AM 1.5G, 1 sun, 4 h), H_2O. Data are presented as mean values ± SD with n = 3.

Catalyst loading (mg)	Evaporation rate (kg m^{-2} h^{-1})	Solar thermal conversion efficiency (%)
blank	0.55 ± 0.11	34.5 ± 7.1
SVG	1.07 ± 0.08	67.1 ± 5.0
0	1.07 ± 0.08	67.7 ± 5.2
0.5	0.99 ± 0.05	62.0 ± 3.1
1	0.99 ± 0.15	62.2 ± 9.4
1.5	0.93 ± 0.16	58.4 ± 10
2	0.95 ± 0.10	59.8 ± 6.2
3	0.87 ± 0.09	54.6 ± 5.5
4	0.88 ± 0.15	55.3 ± 9.4

Supplementary Table 3 | Recent reports on solar vapour generation devices.

Description	Optical absorption (%)	Water evaporation rate (kg m^{-2} h^{-1})	Solar-thermal conversion efficiency (%)	Ref
Carbonaceous materials				
Water splitting photocatalyst deposited on hydrophobic-treated carbon paper	-	0.95	59.8	This work
Bare hydrophobic-treated carbon paper	-	1.07	67.1	This work
Hierarchical porous carbon supported on paper	91	1.52	81.2	[19]
TiN/bio-carbon foam	96	1.47	92.5	[20]
Graphene-nickel foam with PEDOT:PSS coating	97	1.10	73.4	[21]
Carbon nanotube and ultralong hydroxyapatite nanowires bilayer aerogel	96	1.34	89.4	[22]
Melamine-derived carbon sponges with PS thermal insulator	-	1.98	92.0	[23]
Carbon nanotube films	90	3.62 (5 sun irradiation)	45.5	[24]
Plasmonic materials				
Thin-film black gold membrane	91	0.67	57.0	[25]
PVDF membrane with Au-NP top layer	93	1.02	63.1	[26]
Ag/polypyrrole-modified poly(ionic liquid)s hydrogel	96	1.37	88.7	[27]
Pd-NP-decorated bamboo	95	0.96	71.5	[28]
Au nanorods with horn-like protrusions	93	2.70	79.3	[29]
Semiconductor materials				
Self-floating 3-D Ti_2O_3-based aerogels	95	1.31	81.7	[30]
Hollow multi-shelled CuO/Cu_2O	82	3.20	77.0	[31]
$CuFeSe_2$ nanoparticle decorated wood membrane	99	1.04	67.7	[32]
Hierarchical copper silicone nanoscale membrane	94	0.93	58.4	[33]
Polymer materials				
Hierarchically nanostructured gels based on polyvinyl alcohol and polypyrrole	98	3.20	94.0	[34]
Polypyrole-coated sodium alginate-modified poly(divinylbenzene)/polystyrene	90	1.40	87.6	[35]
Polyvinyl alcohol/chitosan/polypyrrole hydrogel	-	3.60	92.0	[36]

Supplementary Table 4 | Recent reports on seawater splitting systems.

Photocatalyst/Electrode	H_2 production rate (μmol g_{cat}^{-1} h^{-1})	Efficiency	Stability (h)	Feedstock/Electrolyte	Sacrificial agent	Ref
Photocatalysis systems						
$RhCrO_x$-Al:$SrTiO_3$ (floating)	1054	0.11% STH	150	Artificial seawater	-	This work
$RhCrO_x$-Al:$SrTiO_3$ (submerged)	355	0.04% STH	66	Artificial seawater	-	This work
Pt/TiO_2 nanoparticles	1476	0.002% STH*	40	Natural Seawater	-	[37]
C-TiO_2/WS_2/ g-C_3N_4	1199	5.06 AQE at 420 nm	25	Natural Seawater	Triethanolamine.	[38]
Pt/Hollow tubular g-C_3N_4	6782	6.9% AQE at 420 nm	8	3.5% NaCl solution	Triethanolamine.	[39]
Pt-loaded conjugated molecule PorFN	10800	1.2 h^{-1} TOF	6	2.8% NaCl solution	-	[40]
Carbon dots/CdS nanosheets	4693	12% AQE at 420 nm	100	Natural seawater	Lactic acid.	[41]
CoP/P-doped $Zn_{0.5}Cd_{0.5}S$	3956	-	15	3.2% NaCl solution	Ascorbic acid.	[42]
Ag/TiO_2/SiO_2	816	-	10	3.5% NaCl solution	Glycerol.	[43]
Pt/P-doped g-C_3N_4	11900	12.1% AQE at 420 nm	16	Natural seawater	Triethanolamine.	[44]
$Rh_{2-y}Cr_yO_3$ loaded $(Ga_{1-x}Zn_x)(N_{1-x}O_x)$	1000	-	5	Artificial seawater	-	[45]
ZnO(nanorod)/Pt/$Cd_{0.8}Zn_{0.2}S$	23700	-	-	Natural seawater	Benzoyl alcohol/acetic acid.	[46]
Photoelectrochemical systems						
Bi-BiOI – TiO_2 nanotube arrays	-	2.21% STH	16	0.1 M Na_2S + 0.2 M Na_2SO_3, 3.5 % NaCl solution.	-	[47]
$RhCrO_x$/p-GaN/InGaN/CoO_x	6.15×10^6	1.9% STH	3	Artificial seawater	-	[48]
Fe_2O_3/TiO_2 – Pt	-	0.49% STH	72	1.0 M NaOH, 3.5% NaCl solution.	-	[49]
RhO_2/$BiVO_4$:Mo – Pt	-	0.6% STH	4.5	Natural seawater.	-	[50]
n-ZnSe/n-Ag_8SnS_6 – Pt	-	0.74% STH	0.8	0.5 M NaCl solution.	-	[51]
Photovoltaic-electrochemical systems						
Si SC + NiFe/ NiS_x-Ni – Ni-NiO-Cr_2O_3	-	11.9% STH	1000	1.0 M KOH with 0.5 M NaCl solution.	-	[52]
InGaP/GaAs/Ge + MHCM-z-BCC/NiMoS	-	17.9% STH	100	Neutral-buffered seawater.	-	[53]
Si SC + NiFeOOH – $(Co,Fe)PO_4$	-	12.8% STH	50	1.0 M KOH, natural seawater.	-	[54]
Si SC NiCoS – NiMoS	-	15.13% STH	14	1.0 M KOH, natural seawater.	-	[55]
Si SC Karst Ni foam – karst Ni foam	-	16.5% STH	24	1.0 M phosphate-buffered solution, natural seawater.	-	[56]

* Calculated assuming AM1.5G irradiation was used.

Supplementary Table 5 | Oxygen characterization for SVG-PC under different conditions. The experiments were carried out in a N_2-filled glovebox to avoid any O_2 leakage from the surrounding to the reactor. O_2 evolution was monitored by a NeoFox-GT fluorometer and Fospor-R fluorescence oxygen sensor probe from Ocean Optics and H_2 was monitor using GC. Note that O_2 measurements were performed under a different light source with modifications to the experimental setup, leading to slight differences in performance between O_2 measurement experiments and the other experiments. n.d. – not detected (below the instrument detection limit). Data for SVG-PC over H_2O and seawater are presented as mean values ± SD with n = 2.

Sample	Feedstock	nH_2 (μmol cm^{-2})	nO_2 (μmol cm^{-2})
Glass-PC	H_2O	39.1	10.5
	Seawater	9.9	n.d.
Untreated SVG-PC	H_2O	38.2	23.1
	Seawater	16.8	12.5
SVG-PC	H_2O	44.1 ± 8.3	25.6 ± 3.3
	Seawater	43.5 ± 4.3	20.6 ± 2.6
	IPA	33.6	14.1
	Turbid	21.5	9.3
	River Cam	33.7	13.4

Supplementary Table 6 | Sample time course of H_2 evolution using SVG-PC floating on pure water and seawater. Conditions: 2.0 mg $RhCrO_x$-Al:$SrTiO_3$ deposited on hydrophobic-treated SVG, irradiation (AM 1.5G, 1 sun, 22 h), H_2O or artificial seawater. Data are presented as mean values ± SD with n = 3.

Feedstock	Time (h)	H_2 (μmol cm^{-2})
H_2O	2	2.56 ± 0.09
	4	7.30 ± 0.32
	8	15.8 ± 0.65
	22	46.7 ± 9.3
Seawater	2	3.49 ± 0.53
	4	7.00 ± 0.87
	8	14.0 ± 0.82
	22	39.1 ± 4.89

Supplementary Table 7 | H_2 evolution rate of SVG-PC under UV and Vis-NIR light. Photocatalytic measurements were performed over pure water for 22 h. n.d. – not detected. Data are presented as mean values ± SD with n = 3.

Light condition	H_2 (mmol m^{-2} h^{-1})	STH (%)
UV only	13.0 ± 0.65	0.08 ± 0.004
Vis-NIR only	n.d.	n.d.

Supplementary Table 8 | Water evaporation rate of SVG-PC and SVG under UV irradiation. Conditions: UV irradiation, 4 h, H_2O. Data are presented as mean values ± SD with n = 3.

Sample (mg)	Evaporation rate (kg m^{-2} h^{-1})
blank	0.29 ± 0.02
SVG	0.56 ± 0.07
SVG-PC	0.59 ± 0.07

Supplementary Table 9 | H_2 evolution of SVG-PC floating directly on and suspended over seawater. Photocatalytic experiments were performed under AM 1.5G, 22 h, at room temperature. Data are presented as mean values ± SD with n = 3.

Light condition	H_2 (mmol m^{-2} h^{-1})	STH (%)
Floating	17.8 ± 2.2	0.11 ± 0.02
Suspended	2.03 ± 0.56	0.009 ± 0.002

Supplementary Table 10 | Photocatalytic performance of Glass-PC, Untreated SVG-PV and SVG-PC in various wastewater sources. Conditions: 2.0 mg $RhCrO_x$-Al:$SrTiO_3$ deposited on glass, SVG, hydrophobic-treated SVG, or suspended directly in liquid, irradiation (AM 1.5G, 1 sun, 22 h), H_2O or artificial seawater. Data are presented as mean values ± SD with n = 3.

Sample	Feedstock	H_2 (mmol m^{-2} h^{-1})	STH (%)
Glass-PC	H_2O	25.9 ± 3.80	0.17 ± 0.02
	Seawater	6.36 ± 0.30	0.04 ± 0.002
Untreated SVG-PC	H_2O	17.6 ± 1.80	0.12 ± 0.01
	Seawater	6.28 ± 0.93	0.04 ± 0.01
SVG-PC	H_2O	21.2 ± 4.20	0.13 ± 0.03
	Seawater	17.8 ± 2.20	0.11 ± 0.02
	River water	19.8 ± 1.50	0.13 ± 0.01
	Turbid waste	18.9 ± 0.46	0.12 ± 0.003
Suspended-PC	H_2O	20.4 ± 4.90	0.13 ± 0.03

Supplementary Table 11 | ICP-OES analysis showing content of various elements in distillate produced from various wastewater sources.

Water source	Element content (ppm)											
	Raw						Purified					
	Na	K	Ca	Mg	S	Si	Na	K	Ca	Mg	S	Si
Seawater	30816	952	1304	2544	1462	3172	9.11	0.09	n.d.	n.d.	0.14	9.41
River water	77.30	5.68	142.78	5.25	20.53	53.00	8.78	0.05	n.d.	n.d.	0.04	8.60
Turbid waste	21028	4048	462	80	380	5064	9.07	0.09	0.04	n.d.	0.12	9.66

Supplementary Table 12 | Photocatalytic performance of SVG-PC under different light intensities. Conditions: 2.0 mg $RhCrO_x$-Al:$SrTiO_3$ deposited on hydrophobic-treated SVG, irradiation (22 h), artificial seawater. Data are presented as mean values ± SD with n = 3.

Light intensity (sun)	H_2 (mmol m^{-2} h^{-1})	STH (%)	Evaporation rate (kg m^{-2} h^{-1})
1.5	32.6 ± 2.49	0.14 ± 0.01	1.58 ± 0.12
1	17.8 ± 2.20	0.11 ± 0.02	0.95 ± 0.10
0.7	9.00 ± 0.85	0.08 ± 0.01	0.81 ± 0.13
0.5	5.31 ± 0.53	0.07 ± 0.01	0.62 ± 0.03
0.2	1.71 ± 0.13	0.06 ± 0.004	0.55 ± 0.02

Supplementary Table 13 | Long-term photocatalytic performance of Glass-PC, untreated SVG-PC and SVG-PC in pure water and simulated seawater. Conditions: 2.0 mg $RhCrO_x$-Al:$SrTiO_3$ deposited on glass, SVG or hydrophobic-treated SVG, irradiation (AM 1.5G, 1 sun, 22 h per cycle), reactors re-purged with N_2 containing 2% CH_4 between cycles.

Sample	Feedstock	H_2 (μmol)						
		Cycle 1	Cycle 2	Cycle 3	Cycle 4	Cycle 5	Cycle 6	Cycle 7
Glass-PC	H_2O	73.10	61.22	45.06	43.69	42.50	48.96	36.75
	Seawater	13.74	10.54	11.59	9.56	9.60	8.61	10.47
Untreated SVG-PC	H_2O	50.85	53.45	53.29	58.34	59.57	47.85	45.37
	Seawater	8.08	12.83	1622	7.54	7.17	6.77	5.48
SVG-PC	H_2O	47.68	50.09	54.66	53.34	56.52	56.99	51.41
	Seawater	47.63	43.80	52.65	48.13	40.98	41.30	37.87

Supplementary Table 14 | Integrated H_2 and clean water production rate of SVG-PC under AM 1.5G irradiation and natural sunlight. Conditions: 2.0 mg $RhCrO_x$-$SrTiO_3$:Al deposited on hydrophobic-treated SVG, river water. The values are the average of duplicate experiments. Data are presented as mean values ± SD with n = 2.

Light conditions	H_2 (mmol m^{-2} h^{-1})	Evaporation rate (kg m^{-2} h^{-1})
AM 1.5G	16.1 ± 3.64	0.94 ± 0.12
Natural sunlight	7.82 ± 1.52	0.71 ± 0.12

Supplementary Table 15 | Techno-economic analysis of floating photothermal-photocatalyst sheet and particulate photocatalyst water splitting panel systems.

Floating photothermal-photocatalyst sheets [a]	$	Particulate photocatalyst water splitting panels [a]	$
Expenditure			
Capital			
Reactor subassembly [9]	6,022,872	Reactor subassembly	6,022,872
Solar vapour generator [57]	104,915	Glass panels [58]	28,000
Gas separation and storage [13]	1,142,860	Gas separation and storage	1,142,860
Piping [9]	104,861	Piping	104,861
Control system [9]	319,862	Control system	319,862
Land [14]	94,055	Land	457,107
Subtotal	**7,789,425**		**8,075,562**
Operation (over 20-year span)			
Operating labour [59]	1,051,200	Operating labour	1,051,200
Power usage [12]	2,106,636	Power usage	2,106,636
Maintenance and repair [60]	389,471	Maintenance and repair	403,778
Subtotal	**3,447,307**		**3,561,614**
Consumables (over 20-year span)			
Photocatalyst[b] [61–63]	49,990	Photocatalyst	19,995
		Pure water [64]	6,307,200
Consumables subtotal	**49,990**		**6,327,195**
Expenditure subtotal	**11,286,722**		**17,964,371**
Revenue (over 20-year span)			
H_2 [c]	14,235,000		14,235,000
Revenue subtotal	**14,235,000**		**14,235,000**
Net	**2,948,278**		**-3,729,371**

[a] STH of 10%, capacity of 1 tonne per day of H_2, average solar insolation of 0.24 kW m^{-2}, facility lifetime of 20 years.[9,11,65]

[b] CoP-modified graphitic carbon nitride was used as a model photocatalyst.[15–17]

[c] Estimated from market price of H_2 and tax credits available for green H_2 production.[66]

Supplementary Table 16 | Photocatalytic performance of SVG-PC with different $RhCrO_x$-Al:$SrTiO_3$ loading for overall solar water splitting. Conditions: $RhCrO_x$-Al:$SrTiO_3$ deposited on untreated SVG, irradiation (AM 1.5G, 1 sun, 22 h), H_2O. Data are presented as mean values ± SD with n = 3.

Catalyst loading (mg)	H_2 (mmol g_{cat}^{-2} h^{-1})	H_2 (mmol m^{-2} h^{-1})	STH (%)
0	n.d	n.d	-
0.5	1.14 ± 0.29	5.22 ± 1.20	0.034 ± 0.01
1	1.40 ± 0.12	11.1 ± 1700	0.073 ± 0.01
1.5	1.19 ± 0.10	14.3 ± 1.90	0.094 ± 0.01
2	1.20 ± 0.95	17.6 ± 1.80	0.11 ± 0.01
3	0.78 ± 0.63	18.9 ± 4.10	0.12 ± 0.03
4	0.67 ± 0.06	20.6 ± 3.70	0.13 ± 0.02

Supplementary Table 17 | Photocatalytic performance of SVG-PC after treatment with DCDMS solution with different silane content. Conditions: 2.0 mg $RhCrO_x$-Al:$SrTiO_3$ deposited on SVG, irradiation (AM 1.5G, 1 sun, 22 h), artificial seawater. Data are presented as mean values ± SD with n = 3.

Silane content (%)	H_2 (mmol m^{-2} h^{-1})	STH (%)
0	6.28 ± 0.93	0.04 ± 0.01
0.5	7.19 ± 2.10	0.05 ± 0.01
1.0	9.75 ± 2.80	0.06 ± 0.02
2.5	17.8 ± 2.20	0.11 ± 0.02
5.0	9.04 ± 4.10	0.06 ± 0.03

Supporting References

1. Zhao, Z., Willard, E. J., Li, H., Wu, Z., Castro, R. H. R. & Osterloh, F. E. Aluminum enhances photochemical charge separation in strontium titanate nanocrystal photocatalysts for overall water splitting. *J. Mater. Chem. A* **6,** 16170–16176 (2018).
2. Phoon, B. L., Lai, C. W., Juan, J. C., Show, P. & Pan, G.-T. Recent developments of strontium titanate for photocatalytic water splitting application. *Int. J. Hydrogen Energy* **44,** 14316–14340 (2019).
3. Goto, Y., Hisatomi, T., Goto, Y., Hisatomi, T., Wang, Q., Higashi, T. & Ishikiriyama, K. A Particulate Photocatalyst Water-Splitting Panel for Large-Scale Solar Hydrogen Generation A Particulate Photocatalyst Water-Splitting Panel for Large-Scale Solar Hydrogen Generation. *Joule* **2,** 509–520 (2018).
4. Takata, T., Jiang, J., Sakata, Y., Nakabayashi, M., Shibata, N., Nandal, V., Seki, K., Hisatomi, T. & Domen, K. Photocatalytic water splitting with a quantum efficiency of almost unity. *Nature* **581,** (2020).
5. Nishiyama, H., Yamada, T., Nakabayashi, M., Maehara, Y., Yamaguchi, M., Kuromiya, Y., Nagatsuma, Y., Tokudome, H., Akiyama, S., Watanabe, T., Narushima, R., Okunaka, S., Shibata, N., Takata, T., Hisatomi, T. & Domen, K. Photocatalytic solar hydrogen production from water on a 100-m 2 scale. *Nature* **598,** 304–307 (2021).
6. Dingenen, F. & Verbruggen, S. W. Tapping hydrogen fuel from the ocean: A review on photocatalytic, photoelectrochemical and electrolytic splitting of seawater. *Renew. Sustain. Energy Rev.* **142,** 110866 (2021).
7. Domen, K., Naito, S., Onishi, T., Tamaru, K. & Soma, M. Study of the photocatalytic decomposition of water vapor over a NiO-SrTiO3 catalyst. *J. Phys. Chem.* **86,** 3657–3661 (1982).
8. Shearer, C. J., Hisatomi, T., Domen, K. & Metha, G. F. Gas phase photocatalytic water splitting of moisture in ambient air: Toward reagent-free hydrogen production. *J. Photochem. Photobiol. A Chem.* **401,** 112757 (2020).
9. Pinaud, B. A., Benck, J. D., Seitz, L. C., Forman, A. J., Chen, Z., Deutsch, T. G., James, B. D., Baum, K. N., Baum, G. N., Ardo, S., Wang, H. & Jaramillo, T. F. Technical and economic feasibility of centralized facilities for solar hydrogen production via photocatalysis and photoelectrochemistry. *Energy Environ. Sci.* **6,** 1983–2002 (2013).

10. Shaner, M. R., Atwater, H. A., Lewis, N. S. & Mcfarland, E. W. A comparative technoeconomic analysis of renewable hydrogen production using solar energy. *Energy Environ. Sci.* **9,** 2354–2371 (2016).
11. Alsayegh, S., Johnson, J. R., Ohs, B. & Wessling, M. Methanol production via direct carbon dioxide hydrogenation using hydrogen from photocatalytic water splitting: Process development and techno-economic analysis. *J. Clean. Prod.* **208,** 1446–1458 (2019).
12. Uekert, T., Pichler, C. M., Schubert, T. & Reisner, E. Solar-driven reforming of solid waste for a sustainable future. *Nat. Sustain.* **4,** 383–391 (2021).
13. Pornrungroj, C., Andrei, V., Rahaman, M., Uswachoke, C., Joyce, H. J., Wright, D. S. & Reisner, E. Bifunctional Perovskite-BiVO 4 Tandem Devices for Uninterrupted Solar and Electrocatalytic Water Splitting Cycles. *Adv. Funct. Mater.* **31,** (2021).
14. Ereev, S. Y. & Patel, M. K. Standardized cost estimation for new technologies (SCENT) - methodology and tool. *J. Bus. Chem.* **9,** (2012).
15. Yi, S., Yan, J., Wulan, B., Li, S., Liu, K. & Jiang, Q. Noble-metal-free cobalt phosphide modified carbon nitride: An efficient photocatalyst for hydrogen generation. *Appl. Catal. B Environ.* **200,** 477–483 (2017).
16. Wang, Y., Zhao, D., Deng, H., Li, M., Chen, J. & Shen, S. Theoretical Insights into the Limitation of Photocatalytic Overall Water Splitting Performance of VIA Group Elements Doped Polymeric Carbon Nitride: A Density Functional Theory Calculation Predicting Solar-to-Hydrogen Efficiency. *Sol. RRL* **5,** (2021).
17. Shcherban, N. D., Aho, A., Sergiienko, S. A., Yaremov, P. S., Eränen, K. & Murzin, D. Y. Melamine-derived graphitic carbon nitride as a new metal-free catalyst for Knoevenagel condensation of benzaldehyde with ethylcyanoacetate. *Catal. Sci. Technol.* **8,** 2928–2937 (2018).
18. Fang, W., Zhao, L., He, X., Chen, H., Li, W., Zeng, X. & Chen, X. Carbonized rice husk foam constructed by surfactant foaming method for solar steam generation. *Renew. Energy* **151,** 1067–1075 (2020).
19. Liu, F., Wang, L., Bradley, R., Zhao, B. & Wu, W. Highly efficient solar seawater desalination with carbons derived from halogen-containing polymers. *RSC Adv.* **9,** 29414–29423 (2019).
20. Guo, D. & Yang, X. Highly efficient solar steam generation of low cost TiN/bio-carbon

foam. *Sci. China Mater.* **62,** 711–718 (2020).

21. Gong, B., Yang, H., Wu, S., Xiong, G., Yan, J. & Cen, K. Graphene Array-Based Anti-fouling Solar Vapour Gap Membrane Distillation with High Energy Efficiency. *Nano-Micro Lett.* **11,** 1–14 (2019).
22. Qin, D., Zhu, Y., Chen, F. & Yang, R. Self- floating aerogel composed of carbon nanotubes and ultralong hydroxyapatite nanowires for highly efficient solar energy-assisted water purification. *Carbon N. Y.* **150,** 233–243 (2019).
23. Gong, F. (Frank), Li, H., Wang, W., Huang, J. & David, D. Scalable , eco-friendly and ultrafast solar steam generators based on one-step melamine-derived carbon sponges toward water purification. *Nano Energy* **58,** 322–330 (2019).
24. Wang, X., He, Y., Liu, X. & Zhu, J. Enhanced direct steam generation via a bio-inspired solar heating method using carbon nanotube films. *Powder Technol.* **321,** 276–285 (2017).
25. Bae, K., Kang, G., Cho, S. K., Park, W., Kim, K. & Padilla, W. J. Flexible thin-film black gold membranes with ultrabroadband plasmonic nanofocusing for efficient solar vapour generation. *Nat. Commun.* **6,** (2015).
26. Li, T., Fang, Q., Lin, H. & Liu, F. Enhancing solar steam generation through manipulating the heterostructure of PVDF membranes with reduced re fl ection and conduction †. *J. Mater. Chem. A* **7,** 17505–17515 (2019).
27. Xiao, C., Liang, W., Hasi, Q., Chen, L., He, J., Liu, F., Wang, C., Sun, H., Zhu, Z. & Li, A. Ag/polypyrrole co-modified poly (ionic liquid)s hydrogels as efficient solar generators for desalination. *Mater. Today Energy* **16,** (2020).
28. Sheng, C., Yang, N., Yan, Y., Shen, X., Jin, C., Wang, Z. & Sun, Q. Bamboo decorated with plasmonic nanoparticles for efficient solar steam generation. *Appl. Therm. Eng.* **167,** 114712 (2020).
29. Huang, Z., Li, S., Cui, X., Wan, Y., Xiao, Y., Tian, S., Wang, H., Li, X., Zhao, Q. & Lee, C. A broadband aggregation-independent plasmonic absorber for highly efficient solar steam generation. *J. Mater. Chem. A* (2020). doi:10.1039/D0TA01980A
30. Li, W., Jian, H., Wang, W. & Yu, D. Highly efficient solar vapour generation via self-floating three-dimensional Ti2O3-based aerogels. *Colloids Surfaces A Physicochem. Eng. Asp.* **634,** 128031 (2022).
31. Chen, X., Li, P., Wang, J., Wan, J., Yang, N., Xu, B., Tong, L. & Gu, L. Multishelled

CuO/Cu2O induced fast photo-vapour generation for drinking water. *Nano Res.* **15,** 4117–4123 (2022).

32. Liu, H., Chen, C., Wen, H., Guo, R., Williams, N. A., Wang, B., Chen, F. & Hu, L. Narrow bandgap semiconductor decorated wood membrane for high-efficiency solar-assisted water purification. *J. Mater. Chem. A* 18839–18846 (2018). doi:10.1039/c8ta05924a
33. Song, X., Song, H., Xu, N., Yang, H. & Zhou, L. Omnidirectional and effective salt-rejecting absorber with rationally designed nanoarchitecture for efficient and durable solar vapour generation. *J. Mater. Chem. A* **6,** 22976–22986 (2018).
34. Zhao, F., Zhou, X., Shi, Y., Qian, X., Alexander, M., Zhao, X., Mendez, S., Yang, R., Qu, L. & Yu, G. Highly efficient solar vapour generation via hierarchically nanostructured gels. *Nat. Nanotechnol.* **13,** 489–496 (2018).
35. He, J., Zhao, G., Mu, P., Wei, H., Su, Y., Sun, H. & Zhu, Z. Scalable fabrication of monolithic porous foam based on cross-linked aromatic polymers for efficient solar steam generation. *Sol. Energy Mater. Sol. Cells* **201,** (2019).
36. Zhou, X., Zhao, F., Guo, Y., Rosenberger, B. & Yu, G. Architecting highly hydratable polymer networks to tune the water state for solar water purification. *Sci. Adv.* **5,** (2019).
37. Zhang, J., Lei, Y., Cao, S., Hu, W., Piao, L. & Chen, X. Photocatalytic hydrogen production from seawater under full solar spectrum without sacrificial reagents using TiO2 nanoparticles. *Nano Res.* **15,** 2013–2022 (2022).
38. Yang, C., Qin, J., Rajendran, S., Zhang, X. & Liu, R. WS2 and C-TiO2 Nanorods Acting as Effective Charge Separators on g-C3N4 to Boost Visible-Light Activated Hydrogen Production from Seawater. *ChemSusChem* **11,** 4077–4085 (2018).
39. Guo, F., Chen, Z., Shi, Y., Cao, L., Cheng, X., Shi, W., Chen, L. & Lin, X. A ragged porous hollow tubular carbon nitride towards boosting visible-light photocatalytic hydrogen production in water and seawater. *Renew. Energy* **188,** 1–10 (2022).
40. Yang, X., Hu, Z., Yin, Q., Shu, C., Jiang, X. & Zhang, J. Water-Soluble Conjugated Molecule for Solar-Driven Hydrogen Evolution from Salt Water. *Adv. Funct. Mater.* **29,** (2019).
41. Zhu, C., Liu, C., Fu, Y., Gao, J., Huang, H., Liu, Y. & Kang, Z. Environmental Construction of CDs/CdS photocatalysts for stable and efficient hydrogen production in

water and seawater. *Appl. Catal. B Environ.* **242,** 178–185 (2019).

42. Chew, Y., Ng, B., Tang, J., Tan, L. & Chai, S. A Synergistic Combination of P-doped Zn0.5Cd0.5S and CoP for Dual-Stage Electron Trapping and Its Application in Seawater Splitting. *Sol. RRL* **5,** (2021).
43. Gao, M., Connor, P. K. N. & Ho, G. W. Plasmonic photothermic directed broadband sunlight harnessing for seawater catalysis and desalination. *Energy Environ. Sci.* **9,** (2016).
44. Wang, C., Yang, C., Qin, J., Rajendran, S. & Zhang, X. A facile template synthesis of phosphorus-doped graphitic carbon nitride hollow structures with high photocatalytic hydrogen production activity. *Mater. Chem. Phys.* **275,** (2022).
45. Maeda, K., Masuda, H. & Domen, K. Effect of electrolyte addition on activity of (Ga1−xZnx)(N1−xOx) photocatalyst for overall water splitting under visible light. *Catal. Today* **147,** 173–178 (2009).
46. Ayyub, M. M., Chhetri, M., Gupta, U., Roy, A. & Rao, C. N. R. Photochemical and Photoelectrochemical Hydrogen Generation by Splitting Seawater. *Chem. - A Eur. J.* **24,** 18455–18462 (2018).
47. Li, F., Dong, B. & Feng, S. Bi shell-BiOI core microspheres modified TiO2 nanotube arrays photoanode: Improved effect of Bi shell on photoelectrochemical hydrogen evolution in seawater. *Int. J. Hydrogen Energy* **44,** 29986–29999 (2019).
48. Guan, X., Chowdhury, F. A., Pant, N., Guo, L., Vayssieres, L. & Mi, Z. Efficient Unassisted Overall Photocatalytic Seawater Splitting on GaN-Based Nanowire Arrays. *J. Phys. Chem. C* **122,** 13797–13802 (2018).
49. Barreca, D., Carraro, G., Gasparotto, A., Maccato, C., Warwick, M. E. A., Kaunisto, K., Sada, C., Turner, S., Gönüllü, Y., Ruoko, T., Borgese, L. & Bontempi, E. Fe2O3 – TiO2 Nano-heterostructure Photoanodes for Highly Efficient Solar Water Oxidation. *Adv. Mater. Interfaces* **2,** (2020).
50. Luo, W., Yang, Z., Li, Z., Zhang, J., Jiangua, L., Zhao, Z., Wang, Z., Yan, S., Yu, T. & Zhigang, Z. Solar hydrogen generation from seawater with a modified BiVO4 photoanode. *Energy Environ. Sci.* **4,** 4046–4051 (2011).
51. Cheng, K. Stable photoelectrochemical salt-water splitting using the n-ZnSe/n-Ag8SnS6 photoanodes with the nanoscale surface state capacitances. *J. Taiwan Inst. Chem. Eng.* **87,**

182–195 (2018).

52. Kuang, Y., Kenney, M. J., Meng, Y., Hung, W., Liu, Y. & Erick, J. Solar-driven, highly sustained splitting of seawater into hydrogen and oxygen fuels. *Proc. Natl. Acad. Sci. U. S. A.* **116,** 6624–6629 (2019).
53. Hsu, S., Miao, J., Zhang, L., Gao, J., Wang, H., Tao, H., Hung, S., Vasileff, A., Qiao, S. Z. & Liu, B. An Earth-Abundant Catalyst-Based Seawater Photoelectrolysis System with 17 .9% Solar-to-Hydrogen Efficiency. *Adv. Mater.* **30,** (2018).
54. Kim, C., Lee, S., Kim, S. H., Park, J., Kim, S., Kwon, S., Bae, J., Park, Y. S. & Kim, Y. Cobalt – Iron – Phosphate Hydrogen Evolution Reaction Electrocatalyst for Solar-Driven Alkaline Seawater Electrolyzer. *Nanomaterials* **11,** 2989–3002 (2021).
55. Wang, C., Zhu, M., Cao, Z., Zhu, P., Cao, Y., Xu, X., Xu, C. & Yin, Z. Environmental Heterogeneous bimetallic sulfides based seawater electrolysis towards stable industrial-level large current density. *Appl. Catal. B Environ.* **291,** 120071 (2021).
56. Gao, X., Chen, Y., Sun, T., Huang, J., Zhang, W., Wang, Q. & Cao, R. Karst landform-featured monolithic electrode for water electrolysis in neutral media †. *Energy Environ. Sci.* **13,** 174–182 (2020).
57. Alibaba. High Performance carbon Graphite Plate/Graphite Sheet For Industries. at <https://www.alibaba.com/product-detail/Customized-Electrode-High-Pure-Conductive-High_1600151269841.html?spm=a2700.galleryofferlist.normal_offer.d_title.411431f6ySMRTl>
58. Alibaba. Window glass. at <https://www.alibaba.com/product-detail/euro-grey-float-glass-for-window_62112300143.html?spm=a2700.galleryofferlist.normal_offer.d_title.5b49740fuEjnLZ>
59. Sara, H. R., Enrico, B., Mauro, V., Andrea, D. C. & Vincenzo, N. Techno-economic analysis of hydrogen production using biomass gasification -A small scale power plant study. *Energy Procedia* **101,** 806–813 (2016).
60. Lauer, M. Methodology Guideline on Techno Economic Assessment (TEA). *Gener. Framew. Therm. WP3B Econ.* (2008).
61. Alibaba. High Quality 99.8% Melamine. at <https://www.alibaba.com/product-detail/High-Quality-99-8-Melamine-

White_1600431176596.html?spm=a2700.galleryofferlist.topad_creative.d_title.61907e60v5yiHV>

62. Sigma-Aldrich. Cobalt(II) hydroxide (CAS No.: 21041-93-0). at <https://www.sigmaaldrich.com/GB/en/product/aldrich/342440>
63. Sigma-Aldrich. Sodium hypophosphite (CAS No.: 7681-53-0). at <https://www.sigmaaldrich.com/GB/en/substance/sodiumhypophosphite87987681530?gclid=Cj0KCQjwz96WBhC8ARIsAATR252e22Z7T41K2bP_zRhyvlElR1GeJZ176sLTjQH7QcA_LysfSO2tRr0aAhpWEALw_wcB>
64. Waternation. Industrial Grade Deionised/Demineralised Water. at <https://waternation.co.uk/product/1000l-industrial-grade-deionised-demineralised-water-container-ownership-ibc/>
65. Shaner, M. R., Atwater, H. A., Lewis, S. & Mcfarland, E. W. A comparative technoeconomic analysis of renewable hydrogen production using solar energy. *Energy Environ. Sci.* **9,** 2354–2371 (2016).
66. International Renewable Energy Agency. *Green Hydrogen Cost Reduction - Scaling up electrolysers to meet the 1.5°C climate goal*. (2020).

End of Supporting Information